NIH Public Access
Author Manuscript
J Biomed Opt. Author manuscript; available in PMC 2009 November 25.

Published in final edited form as:
J Biomed Opt. 2009 ; 14(2): 024020. doi:10.1117/1.3103325.

Differentiation of Benign and Malignant Breast Tumors by *In-Vivo* Three-Dimensional Parallel-Plate Diffuse Optical Tomography

Regine Choe[*], **Soren D. Konecky**[†], **Alper Corlu**[†], **Kijoon Lee**[‡], **Turgut Durduran**[§], **David R. Busch**[†], **Saurav Pathak**[†], **Brian J. Czerniecki**[¶], **Julia Tchou**[¶], **Douglas L. Fraker**[¶], **Angela DeMichele**[**], **Britton Chance**[††], **Simon R. Arridge**[‡‡], **Martin Schweiger**[‡‡], **Joseph P. Culver**[§§], **Mitchell D. Schnall**[¶¶], **Mary E. Putt**[***], **Mark A. Rosen**[¶¶], and **Arjun G. Yodh**[†]

[*]Department of Physics & Astronomy, University of Pennsylvania, 209 S. 33rd St., Philadelphia, PA, 19104; Electronic address: rgchoe@alumni.upenn.edu

[†]Department of Physics & Astronomy, University of Pennsylvania, 209 S. 33rd St., Philadelphia, PA, 19104

[‡]Division of Bioengineering, School of Chemical and Biomedical Engineering, Nanyang Technological University, Singapore 637457; Department of Physics & Astronomy, University of Pennsylvania, 209 S. 33rd St., Philadelphia, PA, 19104

[§]Department of Physics & Astronomy, University of Pennsylvania, 209 S. 33rd St., Philadelphia, PA, 19104; Department of Radiology, Hospital of the University of Pennsylvania, 3400 Spruce St., Philadelphia, PA 19104

[¶]Department of Surgery, Hospital of the University of Pennsylvania, 3400 Spruce St., Philadelphia, PA 19104

[**]Department of Medicine (Hematology/Oncology), Hospital of the University of Pennsylvania, 3400 Spruce St., Philadelphia, PA 19104

[††]Department of Biophysics & Biochemistry, University of Pennsylvania, 3700 Hamilton Walk, Philadelphia, PA 19104

[‡‡]Department of Computer Science, University College London, Gower Street, London, WCIE 6BT, United Kingdom

[§§]Division of Radiological Sciences, Mallinckrodt Institute of Radiology, Washington University, St. Louis, MO 63110; Department of Physics & Astronomy, University of Pennsylvania, 209 S. 33rd St., Philadelphia, PA, 19104

[¶¶]Department of Radiology, Hospital of the University of Pennsylvania, 3400 Spruce St., Philadelphia, PA 19104

[***]Department of Biostatistics & Epidemiology, University of Pennsylvania, 423 Guardian Drive, Philadelphia, PA 19104

Abstract

We have developed a novel parallel-plate diffuse optical tomography (DOT) system for three-dimensional *in vivo* imaging of human breast tumor based on large optical data sets. Images of oxy-, deoxy-, total-hemoglobin concentration, blood oxygen saturation, and tissue scattering were reconstructed. Tumor margins were derived using the optical data with guidance from radiology reports and Magnetic Resonance Imaging. Tumor-to-normal ratios of these endogenous physiological parameters and an optical index were computed for 51 biopsy-proven lesions from 47 subjects. Malignant cancers (N=41) showed statistically significant higher total hemoglobin, oxy-

NIH-PA Author Manuscript
NIH-PA Author Manuscript
NIH-PA Author Manuscript

NIH-PA Author Manuscript

NIH-PA Author Manuscript

NIH-PA Author Manuscript

hemoglobin concentration, and scattering compared to normal tissue. Furthermore, malignant lesions exhibited a two-fold average increase in optical index. The influence of core biopsy on DOT results was also explored; the difference between the malignant group measured before core biopsy and the group measured more than one week after core biopsy was not significant. Benign tumors (N=10) did not exhibit statistical significance in the tumor-to-normal ratios of any parameter. Optical index and tumor-to-normal ratios of total hemoglobin, oxy-hemoglobin concentration, and scattering exhibited high area under the receiver operating characteristic curve values from 0.90 to 0.99, suggesting good discriminatory power. The data demonstrate that benign and malignant lesions can be distinguished by quantitative three-dimensional DOT.

Keywords

Breast Cancer; Diffuse Optical Tomography; Near Infrared Light; Photon Migration; Optical Mammography

I. INTRODUCTION

Breast cancer is one of the most common cancers among women. Approximately one in eight women in the United States will develop breast cancer, and, of these, about 30% will ultimately die of the disease [1]. Thus early detection and accurate diagnosis of breast cancer are important. Existing clinical methods used for breast cancer screening and diagnosis, however, have drawbacks. X-ray mammography, for example, has an ~22% false negative rate in women under 50 [2] and sometimes cannot accurately distinguish between benign and malignant tumors [3]. Even though the false positive rate of individual mammography is less than 10% [4,5], 18% of women with no breast cancer will have undergone a biopsy after 10 mammograms [5]. Techniques such as ultrasound and magnetic resonance imaging (MRI) are sometimes used in addition to X-ray mammography, but they have limitations such as high cost, low throughput, limited specificity (MRI) and low sensitivity (ultrasound). Thus new methods are needed to detect cancers earlier for treatment, to detect cancers missed by mammography [6–8], to reduce the false-positive rate [4,5], and to monitor tumor progression during cancer therapy.

Near-infrared (NIR) diffuse optical tomography (DOT) and spectroscopy (DOS) are tools that rely on functional processes for contrast and therefore have potential to enhance sensitivity and specificity of breast cancer detection/diagnosis. DOT and DOS utilize non-ionizing low-power near-infrared light and are non-invasive and rapid. These diffuse optical methods measure wavelength-dependent tissue optical absorption coefficients, which in turn provide access to blood dynamics, total hemoglobin concentration (*THC*), tissue blood oxygen saturation (StO_2), water and lipid content. Tissue properties accessible to DOT and DOS techniques have been demonstrably different in tumors compared to normal tissues [9–26]. The microscopic origin of tumor optical absorption contrast has been partially explored through the positive correlation of microvessel density and total hemoglobin concentration [13,27, 28]. Similarly, mean size and volume fraction of the nucleus and nucleolus measured by microscopy have been correlated with light scattering measured by DOT [29]. The optical contrast in rapidly growing tumors is physiologically plausible, since these tissues often exhibit increased vascularity, altered oxygen content and altered cellular structures at the microscopic scale [30–35]. Finally, DOT and DOS are attractive for applications such as cancer therapy that require frequent monitoring of physiological parameters. Thus far, changes in tumor contrast during therapy have exhibited agreement with physiological expectation [18,36] and with observations made by other imaging modalities [19,27,37–39].

To date, optical data from sizable numbers of tumors (i.e. more than 30 tumors) have been reported by several research groups [23–26,40,41]. These results generally indicate that optical

NIH-PA Author Manuscript

NIH-PA Author Manuscript

NIH-PA Author Manuscript

methods are capable of distinguishing lesions from healthy background tissue [42]. Demonstrations of a clear distinction between benign and malignant tumors, however, have been scarce, either due to a lack of benign lesion data [25,40] or to a limited three-dimensional imaging capability [23,24]. Even the systems geared towards three-dimensional (3D) image reconstruction [26,41] have not as yet explored the full capability of diffuse optical tomography. Better characterization of malignant and benign lesions is anticipated through improvements in spatial resolution, instrumentation, reconstruction algorithms and through an increase in spectral information [42]. In order to improve the spatial resolution, for example, the number of source and detector positions covering the whole breast should be very large [43]. DOT also relies heavily on reconstruction algorithm quality for accurate quantification of optical properties; optimization of such algorithms is still an open arena for further development and is a key factor for improved image fidelity.

In this contribution, we report tumor contrast extracted from three-dimensional reconstructions of 51 breast tumors acquired using a parallel-plate DOT system. In addition to measurement geometry, our approach differs from others as a result of its very large data set size with on- and off-axis measurements for full 3D reconstruction, and its highly optimized reconstruction schemes. The reconstruction algorithm employs iterative nonlinear methods for accuracy, multi-spectral data for reliable determination of chromophore concentrations and scattering parameters, parallel computing for speed, and spatially variant regularization for image artifact suppression. Furthermore, in order to avoid complications from image artifacts and lack of optical contrast in some lesions, in this study we have used information from dynamic contrast-enhanced MRI (DCE-MRI) to confirm and assign tumor margins. In total, these strategies improve the extraction of tumor-to-normal optical contrast from 3D oxy-, deoxy-hemoglobin and scattering DOT images.

Briefly, malignant cancer showed statistically significant higher total hemoglobin concentration and scattering compared to normal tissue, with two-fold average increase in an optical index derived from intrinsic optical parameters. We did not observe statistically significant differences due to core biopsy in the malignant cancer group; potential bleeding due to core biopsy did not influence DOT results for those measured more than one week after core biopsy. Total hemoglobin concentration, blood oxygenation and scattering were distinguishably lower in a cyst, whereas the difference between tumor and normal tissues for a fibroadenoma and a lobular carcinoma *in situ* were not apparent. Among many parameters, tumor-to-normal ratios of total hemoglobin concentration, scattering, oxy-hemoglobin and the optical index demonstrated AUC (area under the receiver operating characteristic curve) values higher than 0.9, suggesting good discriminatory power for resolving malignant from benign lesions.

The remainder of this paper is organized as follows. The Methods section provides demographic and histopathologic information about the lesions; it also describes the DOT instrument, the human subject measurement protocol, 3D image reconstruction procedures, procedures for tumor-to-normal DOT parameters extraction and statistical analysis. The Results section presents the data and demonstrates a correlation between DOT and DCE-MR images using a representative case for each lesion type. This section also presents a comparison of tumor-to-normal DOT parameters among benign, malignant and biopsied malignant groups. The Discussion section critiques our analysis method, compares results with other DOT/DOS studies and gives suggestions for future improvements. In addition, supplementary material (appendix) about measurement and analysis details are provided with the paper.

NIH-PA Author Manuscript

NIH-PA Author Manuscript

NIH-PA Author Manuscript

II. METHODS

A. DOT Instrumentation

Our parallel-plate DOT system has been characterized using tissue phantoms simulating the breast with tumors [44]. The system consists of a light source module, a table with a built-in Intralid/Ink fluid tank (i.e. the 'breast box') and a detection module. The light source module is comprised of laser diodes, optical switches and optical fibers. Six near-infrared laser diodes are connected to a 6×1 optical switch, which in turn is connected to a 1×45 optical switch. The forty-five optical fibers from this switch are arranged on a 9×5 grid pattern at the compression plate as seen in Figure 1. Of the six lasers, four (690, 750, 786 and 830 nm) are sinusoidally intensity modulated at 70 MHz for frequency-domain measurements. Out of 47 patients, the first 15 patients were measured using this laser configuration (4 wavelengths). Later, 11 patients were measured with an additional continuous-wave laser at 650 nm, and 23 patients were measured with continuous-wave lasers at 650 and 905 nm. These additional lasers were added to improve separation of chromophore contributions based on findings in references [45,46].

Subjects lie in prone position on the table with breasts positioned inside the breast box, which contains a Intralid/Ink fluid whose optical properties are similar to breast tissue (μ_a = 0.05 cm^{-1} and μ_s'=8 cm^{-1} at 786 nm). The fluid is made with an Intralipid scattering agent and an India ink absorption agent. The breast box is made of black-pigment coated aluminum, with one side replaced by an anti-reflection coated plexiglass viewing window.

The compression plate also contains nine optical fibers in a 3×3 grid for frequency-domain detection. The detection has two measurement modes: a remission frequency-domain measurement mode and a transmission continuous-wave measurement mode. The frequency-domain measurements utilize homodyne techniques [47] to provide an initial estimate of breast bulk optical properties for image reconstruction. Transmission continuous-wave data at the viewing window is collected by a lens-coupled 16-bit CCD camera.

Our DOT instrumentation was designed to provide the large data sets essential for full 3D reconstruction. The lens-coupled CCD in our system contains the largest number of on-axis and off-axis measurements covering the whole breast among three-dimensional DOT instruments [13,14,16,17,20,21,48]. For example, even instruments geared towards 3D reconstruction [26,41] typically have up to ~ 10^3 source-detector pairs whereas our instrument utilizes 4×10^4 source-detector pairs per wavelength for reconstruction. The direct use of a lens-coupled CCD, as opposed to fiber coupling, greatly reduces the calibration coefficient unknowns. The parallel plate transmission geometry with soft compression provides increased light transmission and reduced detection dynamic range linearity requirements compared to other geometries, e.g. the uncompressed conical or ring geometry. The use of Intralid/Ink fluids further reduces dynamic range requirements and ensures good contact between optodes (sources and detectors) and the diffuse medium (i.e. the breast and Intralid/Ink fluid). Finally, our hybrid system permits measurement of bulk optical properties for use as initial guess in our reconstruction. Pure continuous-wave measurement systems [14,20] do not have this capability.

B. DOT Measurement Protocol

All human research was approved by the University of Pennsylvania Institutional Review Board. After informed consent was obtained from each subject, the subject was positioned on the table with both breasts inside the empty breast box. Based on the tumor location identified by palpation or prior radiological information, the breast position with respect to the viewing window was optimized such that the tumor was well within the field of view. Then a soft

NIH-PA Author Manuscript

NIH-PA Author Manuscript

NIH-PA Author Manuscript

compression was applied to hold the breast in a stable position. The compression distance varied between 5.5 and 7.5 cm (6.4 ± 0.5 cm) depending on the breast size. A snapshot of the breast outline was taken by the CCD camera before filling the box with the Intralid/Ink fluid. After filling the box, the diffuse optical image scan was conducted for 8–12 minutes. Typically, we only measured a single breast per subject, most often with a single lesion. After the subject measurements, we filled the breast box completely with Intralid/Ink fluid and covered the top of the box with a slab of silicone phantom to take reference optical measurements. The silicone slab extends the diffuse medium vertically above the breast box, just as the subject's torso extends the diffuse medium in the actual breast measurement.

C. 3D DOT Reconstruction

The near-infrared (NIR) spectra of major tissue chromophores, such as oxygenated hemoglobin (HbO_2), deoxygenated hemoglobin (Hb), water and lipid, are well known [49], and imaging is readily possible because their NIR absorptions are much lower than in visible or infrared spectral regions. The overall tissue absorption coefficient, μ_a, at given wavelength (λ) may be decomposed into linear contributions from major chromophores via the relation:

$$\mu_a(\lambda)=\sum_{l=1}^{L}\varepsilon_l(\lambda)\,C_l+\mu_a^{bg}(\lambda)$$

where L is the total number of chromophores, $\varepsilon_l(\lambda)$ is the extinction coefficient of the lth chromophore, C_l is the concentration of lth chromophore, and μ_a^{bg} is a background absorption coefficient. The scattering coefficient is significantly larger than the absorption coefficient in the NIR, so that the propagation of light is well modeled by the photon diffusion equation [50–52]. The spectral variation of the reduced scattering coefficient is further approximated to have the form, $\mu_s'(\lambda)=A\lambda^{-b}$, a result based on simplified Mie scattering theory. Here A is the scattering prefactor and b is the scattering power which depends on the size and number of the scatterers in the tissue [53,54]. The multi-spectral method utilizes these spectral relations as constraints, using all wavelength data simultaneously to fit for chromophore concentrations and scattering factors directly, rather than first fitting μ_a and μ_s' individually for each λ and then subsequently calculating concentrations C_l [45,46,55].

Using this multi-spectral method, we derived average bulk optical properties of breast based on remission frequency-domain measurements by fitting $C_{\mathrm{Hb}}^{\mathrm{bulk}}$ (breast), $C_{\mathrm{HbO_2}}^{\mathrm{bulk}}$ (breast), A^{bulk}(breast) and b^{bulk}(breast) using an analytic solution of photon diffusion equation for semi-infinite medium. $\mu_a^{bg}(\lambda)$of breast was fixed as combination of 31% water and 57% lipid absorption based on the literature [56–58]. Intralipid/Ink fluid properties $C_{\mathrm{ink}}^{\mathrm{bulk}}$, A^{bulk}(Intralipid) and b^{bulk}(Intralipid) were derived from frequency-domain reference measurements made on the breast box when it was completely filled with an Intralipid/Ink solution.

Then we applied the multi-spectral approach to enhance image reconstruction by reducing the number of unknowns compared to the available measurements [45,46]. This approach enables us to achieve reasonable separation between absorption and scattering even for continuous-wave measurements. The unknowns for reconstruction were $C_{Hb}(\mathbf{r})$, $C_{HbO_2}(\mathbf{r})$, and $A(\mathbf{r})$, where $\mathbf{r}$ represents position within the three-dimensional sample volume. To assess the initial values for these parameters, we segmented the reconstruction volume into a half-ellipsoidal breast region and an Intralid/Ink fluid region based on the breast outline photo. Then initial value for the parameter $C_{Hb}(\mathbf{r})$, $C_{HbO_2}(\mathbf{r})$ were assigned to $C_{\mathrm{Hb}}^{\mathrm{bulk}}$ (breast) and $C_{\mathrm{HbO_2}}^{\mathrm{bulk}}$ (breast) if $\mathbf{r}$ falls into breast region or to zero otherwise. On the other hand, initial value for $A(\mathbf{r})$ were set to A^{bulk}(breast) if $\mathbf{r}$ falls into breast region or A^{bulk}(Intralipid) if it falls into Intralid/Ink fluid region. μ_a^{bg} of the Intralid/Ink fluid region was fixed by the directly measured μ_a of the fluid.

NIH-PA Author Manuscript

NIH-PA Author Manuscript

NIH-PA Author Manuscript

The scattering power was fixed as b^{bulk}(breast) and b^{bulk}(Intralipid) for each region respectively.

For the given set of optical properties, a finite element method based numerical solver [59] was utilized to derive a calculated fluence rate, $\Phi_c(\mathbf{r}_d)$ at detector position $\mathbf{r}_d$, given a set of optical properties. To suppress image artifacts associated with sources and detectors, we used a nonuniform unstructured mesh with higher nodal concentrations at source/detector planes for the finite element method [60]. The measured fluence rate, $\phi_m(\mathbf{r}_d)$, was constructed by down-sampling and smoothing the CCD data on a 41×24 grid (as shown in Figure 1) corresponding to a 3 mm spacing for each detector.

We defined a Rytov-type objective function χ^2 with the Intralid/Ink fluid reference measurements used for normalization (the specific form of χ^2 is given in reference [19] and in the appendix). The unknowns were updated using an iterative conjugate-gradient-based scheme [61] modified to include the multi-spectral approach [45,46]. The iterative nonlinear method is superior to linear methods for quantification, because the inverse problem is intrinsically nonlinear. The memory-efficient conjugate gradient method allowed use of large data sets (10^4 spatial ×6 spectral data). Furthermore, parallel computation was implemented to dramatically speed up reconstruction time.

In order to compensate for higher sensitivity near source/detector planes and lower sensitivity near the sample center, spatially variant regularization [62] was added within the objective function. To find an optimum regularization parameter, α, an initial reconstruction using an envelope-guided regularization technique [63] was performed, first yielding an estimate of the initial regularization parameter, α_0 [64]. Then nine reconstructions were performed with nine different regularization parameters ranging from $0.01\alpha_0$ to $100\alpha_0$ to further optimize this parameter. We examined the L-curve that plots the residual norm (i.e. the sum squared difference between measured and calculated data) versus the image norm (i.e. the sum squared difference between the initial guess and reconstructed optical parameters) to find the optimal regularization parameter.

After the selection of the best $C_{Hb}(\mathbf{r})$, $C_{HbO_2}(\mathbf{r})$ and $A(\mathbf{r})$ images based on the optimal regularization parameter determined by the L-curve analysis, we constructed 3D images of total hemoglobin concentration ($\mathrm{THC}(\mathbf{r}) = C_{Hb}(\mathbf{r}) + C_{HbO_2}(\mathbf{r})$), blood oxygen saturation ($\mathrm{StO_2}(\mathbf{r}) = C_{HbO_2}(\mathbf{r})/\mathrm{THC}(\mathbf{r})$), scattering $\mu_s'(\mathbf{r}, \lambda) = A(\mathbf{r})\lambda^{-b(\mathbf{r})}$, and the overall optical attenuation $\mu_{\mathrm{eff}}(\mathbf{r}) = \sqrt{3\mu_a(\mathbf{r})\mu_s'(\mathbf{r})}$ at 786 nm.

D. Extraction of DOT Tumor Parameters

In order to extract DOT parameters from tumor and healthy regions, additional steps were taken. First, the approximate tumor location was determined based on MR images of the same breast. Each tumor was classified as belonging to the retroareolar region or one of four quadrants (i.e. upper outer, upper inner, lower inner, and lower outer quadrant). The relative proximity of the mass with respect to the nipple and the chestwall was also noted. When MRI was not available, spatial information about the tumor was derived from radiology reports based on X-ray mammograms and ultrasound. Then based on the outline photo of the breast, we determined the position of nipple in the DOT images and then in the corresponding axial DOT slices. We chose to use a $\mu_{eff}(786nm)$ map for tumor segmentation as it represents a combination of absorption and scattering contrast and, therefore, is less sensitive to parameter cross-talk.

The spatial location with maximum intensity of $\mu_{eff}(786nm)$ near the radiologically determined tumor region was marked as the starting point for a 3D region growing algorithm, with cut-off

NIH-PA Author Manuscript

NIH-PA Author Manuscript

NIH-PA Author Manuscript

at full-width-at-half-maximum. When the tumor-to-normal contrast was relatively low, such that the region grew into multiple locations, tumor size extracted either from pathology or radiology reports was used as a limiting factor to stop the growth algorithm. This approach was effective for selection of tumor regions in images while minimizing the influence of artifacts. Since our DOT reconstructions are subject to source and/or detector artifacts, slices near the source and detector planes (up to 8 mm) were excluded from the region growing process. When the tumor was not adequately visible in DOT (e.g. in some fibroadenomas (N=3), lobular carcinomas *in situ* (N=2) and fibrocystic lesions (N=1)), then the lesion region was fixed based on radiological assessment rather than the region growing algorithm. Normal tissue was defined as the breast tissue outside the tumor region based on the following criteria: (1) Slices up to 8 mm from source and detector planes were excluded and (2) regions with μ_{eff} (at 786 nm) outside ± two standard deviations from its average over the entire breast were excluded. These exclusions ensured that source and detector artifacts were removed from the 'average' normal tissue. Note, factors such as different compression schemes and shifts of nipple location due to breast positioning variation were necessarily considered, since the breast is highly deformable organ. MRI, for example, used sagittal compression for breast imaging whereas DOT used axial compression in this study. We averaged the DOT parameters inside the regions defined by the above segmentation (i.e. to obtain mean $\bar{X}_{(T)}$ for the tumor region and mean $\bar{X}_{(N)}$ for the normal region, where X is the optically-derived physiological variable). An optical contrast ratio (i.e. rX, the relative value of X between the tumor and normal tissue) was then defined as in Table I. We also defined an optical index $\mathrm{OI}=\mathrm{rTHC} \times r\mu_s'/\mathrm{rStO_2}$. The rationale for this index was based on the hypothesis that tumor *THC* and scattering increase due to increased angiogenesis and cell proliferation while StO_2 decreases due to hyper-metabolism [25]. Images of relative values of any variable are defined in a similar fashion: $rX(\mathbf{r}) = X(\mathbf{r})/\bar{X}_{(N)}$ and $\mathrm{OI}(\mathbf{r})=\mathrm{rTHC}(\mathbf{r}) \times r\mu_s'(\mathbf{r})/\mathrm{rStO_2}(\mathbf{r})$.

E. Classification of Groups

Only the biopsy-proven lesions from the histopathology report were selected for quantification of optical tumor-to-normal contrast. Lesions were separated into three groups: benign (all benign lesions were measured by DOT before core biopsy), malignant lesions measured before core biopsy (MalBcb), and malignant lesions measured after core biopsy (MalAcb). The separation of malignant lesions into pre- and post-core biopsy groups enabled us to address the concern that bleeding induced by core biopsy might influence DOT. Note, subjects who had fine needle aspiration prior to DOT measurements were included in the pre-core biopsy group (i.e. MalBcb group), since the fine needle aspiration was deemed to have minimal effect. For the MalAcb group, the DOT measurement was carried out more than one week after core biopsy, ensuring some level of healing.

From demographic information, parameters such as age, height, weight, menopausal status, and race were also collected. Body mass index (BMI) was calculated as BMI = weight / height^2 ([kg/m^2]). From the pathology reports, in addition to lesion type, lesion size and modified Bloom and Richardson scores (mBR) were extracted. When the lesion size was not available or was ambiguous in the pathology report, the longest dimension of the lesion was extracted from the radiology report and was taken as the lesion size. Mammographic density information was collected from the radiology reports.

F. Statistical Analysis

Statistical analysis of these data was performed using R 2.6, a statistical computing and graphics software [65]. A type I error rate of 0.05 was used for all hypothesis tests. Demographic data were summarized using means and 95% confidence intervals (CI) for continuous data or percentages for categorical data.

NIH-PA Author Manuscript

NIH-PA Author Manuscript

NIH-PA Author Manuscript

The optical tumor contrast ratios were log-transformed to achieve approximate normality and then analyzed using a mixed effects model [65,66]. In this model, we took into account the potential correlation between measurements taken from multiple lesions in the same breast or in the same women. We fit to a model that estimated the mean optical contrast ratio for each group. After developing 95% CIs using the resulting standard errors, we tested the hypothesis that each optical contrast parameter was unity. Since the bleeding induced by a core biopsy might be expected to influence DOT results, for the malignant group we tested the hypothesis that there were no differences in mean optical contrast ratio associated with receiving/not-receiving a core biopsy. Also, we tested another null hypothesis that there were no differences in mean optical contrast ratios between benign and malignant groups. Finally, we used univariate models to test whether there was an association between optical tumor contrast ratios and clinical covariates including body mass index, menopausal status, lesion size and race. For any variable that showed a significant univariate association, we tested whether the association persisted in a model that also included lesion pathology (i.e. benign or malignant).

Lastly, to assess the capacity of the approach to discriminate between benign and malignant lesions, we constructed logistic regression models using each optical parameter as the predictor in the model. Odds ratios (ORs) were used to estimate the effect sizes, the significance of each effect was assessed using a Wald test, and a receiver operating characteristic (ROC) curve was constructed using the estimates of sensitivity and specificity [67]. An area under the ROC curve (AUC) was calculated for each DOT parameter to serve as a measure of discrimination. Because logistic regression assumes observations are independent, we carried out a sensitivity analysis using a subset of the data where the malignant lesions from two women with a benign lesion were dropped, and where one malignant lesion was dropped from each of the two women with two malignant lesions. This modification to the dataset had negligible impact on the findings presented here. Representative error estimates for sensitivity and specificity were computed using the exact binomial distribution.

III. RESULTS

A. Demographic, Radiologic and Histopathologic Information of Benign and Malignant Lesions

We recruited 60 female subjects for DOT measurement between the years 2001 and 2006. All of these subjects had a clinically suspicious lesion. Subjects with prior mass-removal surgery (N=4) or subjects undergoing neoadjuvant chemotherapy (N=2) were not included in the analysis. Thus, only properties of lesions prior to clinical intervention were probed. Subjects with breast implants (N=1) or with extensive bleeding due to previous core biopsy (N=2) were also excluded from the analysis since these conditions significantly affected DOT signal-to-noise. Subjects with no biopsy results (N=4) were excluded as well. We report on DOT measurements and analyses of forty seven female subjects with biopsy-proven lesions.

Fifty-one lesions from 47 patients were characterized with DOT. Ten patients had benign lesions, and, of these, two patients had an additional malignant lesion. In Table II these patients were assigned to the benign group. A total of 37 patients had exclusively malignant lesions, and of these, two patients had two lesions. No patient had more than two lesions. The demographic information for patients in benign and malignant groups is presented in Table II. Average lesion size along the longest dimension was 1.7 cm for benign and 2.1 cm for malignant lesions, ranging from 0.4 to 9.3 cm. The majority of women in this study were pre-menopausal (60% of benign group, 51% of malignant group) and Caucasians (> 65% both groups) with mean ages of 43 (benign group) to 48 (malignant group). At least half of both groups with known density had heterogeneously dense or extremely dense breasts as determined by X-ray mammography.

NIH-PA Author Manuscript

NIH-PA Author Manuscript

NIH-PA Author Manuscript

The histopathologic diagnosis of these lesions is summarized in Table III. We divided the 51 lesions into three groups: (1) benign, (2) malignant measured by DOT before core biopsy (MalBcb), and (3) malignant measured by DOT after core biopsy (MalAcb). 80% and 95% of the malignant lesions measured before and after core biopsy in this study were invasive ductal carcinoma, while 40% of the benign lesions were fibroadenomas, 30% were cysts, another 30% were lobular carcinoma *in situ* and 10% were fibrocystic disease.

B. Example Images of MRI and DOT

Three representative DOT images are shown in Figure 2, Figure 3, and Figure 4. The top row of each figure provides three images: one sagittal DCE MR image slice at the tumor center, an axial DCE-MR image slice along the horizontal line drawn in the sagittal image, and a three-dimensional depiction of breast outline and tumor region. The axial MRI slice was re-arranged such that the orientation matches with DOT orientation (i.e. caudal-cranial). The DOT slices are arranged to show $rTHC(\mathbf{r})$, $rStO_2(\mathbf{r})$, $rHbO_2(\mathbf{r})$, $rHb(\mathbf{r})$,$r\mu_s'$ at 786nm, and $OI(\mathbf{r})$ along the horizontal line. In order to help with comparison, the color-bar range was fixed throughout the examples for each parameter (e.g. 0.8 – 1.3 for *rTHC* and 0.6 – 2.1 for *OI*).

Clear distinctions between the lesion and surrounding tissue were observed in *rTHC*, $r\mu_s'$ and *OI* images for the invasive carcinoma (Figure 2). Intermediate contrasts were observed for the ductal carcinoma *in situ* (Figure 3) and low contrasts for the fibroadenoma (Figure 4).

Invasive Ductal Carcinoma—The first example is from a 53 year old postmenopausal female with a retroareolar mass in her right breast. DOT measurements were performed before any core biopsy. Dynamic contrast enhanced MR images showed a clear enhancement of Gadolinium uptake signal behind the nipple in Figure 2. The size of the enhancement determined by radiologists was 2.2 cm. The mammographic density of this breast fell into the scattered fibroglandular category. Histopathology analysis after mastectomy revealed a 2.0 cm mixture of invasive ductal carcinoma (with mBR grade of 8) and ductal carcinoma *in situ* behind the nipple.

The compression distance for the DOT measurement of the same subject was 6 cm. The nipple was shifted towards the source plane during DOT positioning, thus the slice best exhibiting the tumor contrast turned out to be the one 1.8 cm away from source plane. As can be seen in Figure 2, DOT slices showed elevated *rTHC*, $r\mu_s'$, $rHbO_2$, *rHb*, and *OI* at the tumor site, slightly displaced towards the lateral side (i.e. the right side of the axial image for right breast) in agreement with the MRI axial slice. The $rStO_2$ slice did not exhibit a localized feature, but rather it showed a broad, slightly low oxygenation region near the tumor location. While elevated values of most parameters were apparent within the tumor site, subtle differences in the images were always found.

Ductal and Lobular Carcinoma *in situ*—The second example is from a 39 year old pre-menopausal female with mixture of ductal carcinoma *in situ* and lobular carcinoma *in situ* in her left breast. X-ray mammography and ultrasound detected a 3 cm mass at 3 o'clock. In DCE-MRI, enhancement spanning 3 – 5 cm appeared around 3–4 o'clock, which corresponds to left upper side of the axial image as shown in Figure 3(b). DOT measurements were performed before core biopsy. The mammographic density of this breast fell into the extremely dense category. Histopathology analysis upon excisional biopsy sample revealed an extensive ductal carcinoma *in situ* with intermediate grade nuclei growing in a solid pattern with focal comedo-type necrosis and extensive lobular carcinoma *in situ*.

The compression distance for the DOT measurement was 6 cm. The nipple was shifted towards the detector plane during DOT positioning, thus the slice at 4.6 cm from source plane was

NIH-PA Author Manuscript

NIH-PA Author Manuscript

NIH-PA Author Manuscript

selected for presentation. In the reconstructed images (Figure 3), three regions with elevated contrast in *rTHC* and $r\mu_s'$ are evident. However, the contrast of each region is much lower than those of the invasive carcinoma shown in Figure 2. The left upper region corresponding to the tumor site exhibited high optical contrast in *rTHC*, $r\mu_s'$ and *OI*. The lower center region corresponds to the nipple showing *rTHC*, $r\mu_s'$, *OI* larger and $rStO_2$ smaller than unity.

Fibroadenoma—The third example is from a 51 year old pre-menopausal female with a fibroadenoma in her left breast. DCE-MRI saw asymmetric density exhibiting some enhancement in the lower outer quadrant (as seen in Figure 4(b) at the left upper side). However, no suspicious finding was identified by ultrasound or from the digital mammogram. DOT measurements were performed before any core biopsy. The mammographic density of this breast was categorized as scattered fibroglandular density. Needle localization biopsy yielded benign breast tissue with a 5 mm fibroadenoma.

In the reconstructed images (from slice 4.6 cm away from source plane) of Figure 4, distinct optical contrast in the expected region was not found. The compression distance for the DOT measurement was 6.5 cm. Since the optical contrast was not apparent, a spherical region was assigned as a benign lesion in DOT images based on the extent of gadolinium enhancement in DCE-MR image, which was substantially larger than the size reported by histopathology. Two regions of high *OI* were notable, but they did not correspond to the fibrosis region identified by MRI.

C. Distinction between Benign and Malignant Lesions based on Optical Tumor Contrast

Figure 5 shows the data for each group while Table IV summarizes, mean values and 95% confidence intervals for optical contrast parameters (*rTHC*, $rStO_2$, $r\mu_s'$, *rHb*, $rHbO_2$,*OI*). A value of 1.0 indicates zero contrast. The benign group exhibited contrast of 0.96 to 1.11 for all parameters, which were not significantly different from 1.0. With the exception of $rStO_2$, the parameter estimates for the malignant lesions in both MalBcb and MalAcb groups were significantly higher than 1.0. Of particular note, mean values of $r\mu_s'$ and *OI* were more than 1.5 and 1.8 for both malignant groups. In no case were significant differences found between mean values of the parameters for the MalBcb and MalAcb groups. The intra-subject tissue variability (σ_Y / Y) was calculated based on the standard deviations of both normal (N) and tumor (T) regions, i.e. $\sigma_Y / Y = \sqrt{(\sigma_{X(N)} / \bar{X}_{(N)})^2 + (\sigma_{X_{(T)}} / \bar{X}_{(T)})^2}$, where $Y = \bar{X}_{(T)} / \bar{X}_{(N)}$. The median intra-subject variability of 51 lesions for *rTHC*, $rStO_2$, $r\mu_s'$, *rHb* and $rHbO_2$ were 9%, 5%, 20%, 10%, and 14%, respectively. This intra-subject variability for each region was not included in the statistical analysis presented in Table IV, since the focus of current study was not the automatic detection of lesion location, but rather on the characterization of lesions with lesion location provided by other imaging modalities. Menopausal status, race, size of lesion did not show an association with any of the optical contrast parameters (data not shown). However, BMI was associated ($P < 0.05$) with both $r\mu_s'$ and *OI* in both univariate models and after adjustment for type of lesion (malignant versus benign). While the effects of BMI were statistically significant for $r\mu_s'$ and *OI*, they were substantially less than the effects of lesion type (data not shown).

Figure 6 shows the ROC curves for *rTHC*, $rHbO_2$, $r\mu_s'$, and *OI*. The ROC curves plot the true positive rate on the vertical axis and the false positive rate on the horizontal axis. For example, for *rTHC*, if we designated a lesion with *rTHC* > 1.06 as malignant, then 40 out of 41 malignant lesions would be correctly identified for a sensitivity (true positive rate) of 98% (95% CI = 87–100%), and 9 out of 10 benign lesions would be correctly identified for a specificity (1 - false positive rate) of 90% (95% CI of wide range: 55–100%). Table V shows the Area under the ROC curve (AUC) and Odds Ratio (OR) values for a lesion to be malignant versus benign

NIH-PA Author Manuscript

NIH-PA Author Manuscript

NIH-PA Author Manuscript

for each optical parameter. All of the parameters except $rStO_2$ and rHb were positively associated with increased odds of malignancy with OR values ranging from 4.3 to 176 per 0.10 (10%) increase in the relative optical parameters. Similarly the AUCs suggested good discriminatory power with values, excluding $rStO_2$ and rHb, of between 0.90 and 0.99. The OR values for $rTHC$, $r\mu_s'$, $rHbO_2$ and OI achieved statistical significance (i.e. $P < 0.05$). However the 95% CIs of ORs were wide. For example the 95% CI for $r\mu_s'$ was from 1.4 to 333, the 95% CI for $rTHC$ was from 3.3 to 9432, and the 95% CI for OI was from 1.3 to 33.3. This indicates substantial uncertainty in the parameter estimates and is a result of the relatively small sample size, particularly the small number of benign lesions (N=10). Additionally, it is important to note that the performance of any of these predictors would weaken if applied to a new validation dataset, since the predictions are based on small number of benign lesions.

IV. DISCUSSION

A. Significance

Several groups have reported measurable differences in the optically-derived properties of breast tumors compared to background tissues [11–14,17,21–24,41]. The research reported herein, however, differs for several reasons, including instrumentation, 3D image reconstruction and lesion definition (i.e. MRI-guided).

Perhaps most importantly, our results compare DOT and dynamic contrast enhanced MRI (DCE-MRI) in a statistically significant number of subjects. Other groups have demonstrated correlation of stand-alone DOT data with (mostly) X-ray mammograms/ultrasound [13,21, 22,29,68,69], or MRI [37,48] for a limited number of subjects. Some groups have measured concurrently with other imaging modalities: MRI [11,70–72], ultrasound [17,27], and 3D tomosynthesis [73,74]. However, most of these concurrent results rely heavily on *a priori* spatial information from the other imaging modality for 3D optical reconstruction. Our ability to reconstruct accurate images without "*a priori*" spatial information is due to our DOT instrumentation and reconstruction algorithm which were designed to provide and utilize the large data sets essential for full 3D reconstruction. The number of on-axis and off-axis measurements of our lens-coupled CCD detection is the largest among among existing three-dimensional DOT instruments [13,14,16,17,20,21,48] (i.e. larger by factors of ~100× or more before downsampling). The 3D DOT reconstructions are based on measurements at multiple optical wavelengths chosen to better separate scattering from absorption and isolate individual chromophore contributions [45,46]. Furthermore, the use of DCE-MR images and radiology reports enable us to better define tumor margins and locations in the diffuse optical images, in some cases reducing ambiguities that would be present had we employed the optical images alone. With these features, we demonstrated clear distinction between benign and malignant tumor optical properties with statistical significance.

B. Comparison of DCE-MRI and DOT images

Dynamic contrast-enhanced MRI using Gadolinium-DTPA (Diethylene triamine pentaacetic acid) stands out among clinical imaging modalities by offering vasculature-sensitive parameters [75,76]. It is therefore a good choice for comparison to DOT. Sometimes tumor contrast is very clear in both Gadolinium enhanced DCE-MRI and in most parameters of DOT (Figure 2). On the other hand, the DOT contrast from benign lesions is often negligible (Figure 4). Furthermore, in some cases, more than one high contrast region appears in the DOT images (Figure 3, Figure 4). Sometimes these high contrast regions are identified as the nipple or as glandular tissue positioned near the detector plane and are also seen in DCE-MRI. These regions exhibit subtle spatial differences among parameters (e.g. the shape or the center of the contrast region) or distinct characteristics when all the parameters are considered together. For example, the nipple in Figure 3 exhibited lower blood oxygen saturation whereas the ductal

NIH-PA Author Manuscript

NIH-PA Author Manuscript

NIH-PA Author Manuscript

carcinoma in situ showed higher StO_2 than the surrounding tissue; both exhibited values higher than unity for *rTHC*, $r\mu_s'$ and $rHbO_2$. Some high contrast regions in DOT reconstructions are not found in DCE-MRI (e.g. Figure 3, Figure 4); these regions could be tissue with a physiologically elevated level of hemoglobins/scattering (but insensitive to DCE-MRI) or they could be DOT image artifacts. Further work is needed to classify these regions and to devise image processing constraints to reduce image artifacts. For now, we have focused our efforts on characterization of tumor-to-normal ratio in order to derive upper bounds about what can be done with optics.

C. Relative Measures and the Optical Index

Our focus on tumor-to-normal ratios rather than absolute properties is driven by the observation that inter-subject absolute optical property variation is quite significant. For example, averaged over the whole breast, reconstructed *THC* varied from 6 – 45 μM and reconstructed μ_s' at 786 nm from 7 – 13 cm^{-1}. Inter-subject variation in absolute optical properties is caused by differences in breast tissue composition. A significant inverse correlation between THC and BMI have been found, for example, across a wide range of DOT/DOS instrumentation and measurement geometries [21,55,77,78]. Higher BMI is indicative of more adipose tissue content wherein the blood supply is smaller than in glandular tissue [34]. In contrast to absolute *THC*, *rTHC* has emerged from our data as robust quantity for tumor contrast regardless of tissue composition. Similarly, $r\mu_s'$ has proven superior to absolute μ_s' for tumor contrast. Evidently relative contrast can remain, even if absolute optical properties shift. It is also desirable to find other tissue optical indices which improve malignancy contrast. This concept has also been used by Cerussi *et al* [40]. Our suggested optical index, $\mathrm{OI}=\frac{\mathrm{rTHC}\times r\mu_s'}{\mathrm{rStO_2}}$, improved tumor contrast and is a logical composite variable based on the hypothesis of tumor hyper-metabolism [25]. It is also less sensitive to absorption-scattering crosstalk.

D. Physiological Origins of Optical Tumor Contrast

Angiogenesis associated with solid tumors of radiologically detectable size [79] likely contributes to high *THC* contrast between breast tumor and normal tissue measured by DOT. DOT is sensitive to vasculature at the microvessel level (i.e. capillaries, arterioles, and venules). Indeed, a positive correlation between microvessel density and *THC* has been found, providing further insight about the microscopic origin of *THC* contrast [13,27,28]. Among various physiological parameters available to DOT and DOS, most groups have reported the high *THC* contrast of malignant tumors [13,14,17,18,21,26,28,80–83].

The origin of scattering contrast of the cancer is more elusive than absorption. Nevertheless, an increase in number density of subcellular organelles (e.g. mitochondria, nucleolus), due to cell proliferation, can increase tissue scattering. Recently, Li *et al* [29] have observed significant differences in the mean size and volume fraction of cellular scattering components (thus scattering coefficients) between benign and malignant lesions. Some groups have reported tumor scattering contrast comparable to ours [29], and some have reported contrast ~20–40 % higher than normal tissue scattering [23,28,81,82]. Because of absorption and scattering crosstalk issues, at the present time there remains some uncertainty about the fidelity of the scattering assignment. In our laboratory, we have shown that it is possible to decouple chromophore concentrations and scattering in continuous-wave data by choosing optimal wavelengths [45,46]. However, our current system does not utilize all the optimal wavelengths. According to simulations using the experimental wavelength set, reconstructed *rTHC* was often underestimated while $r\mu_s'$ was often overestimated by 10–20% (data not shown). The overall influence on the optical index was a 10% underestimation. Thus, even though our wavelengths

NIH-PA Author Manuscript

NIH-PA Author Manuscript

NIH-PA Author Manuscript

were sub-optimal, the resulting parameter crosstalk does not appear to influence the major findings of this study.

Our measurements of StO_2 contrast were not compelling. Cancer oxygen metabolism may depend strongly on the cancer stage and biochemical pathways involved. Also, changes in blood oxygenation may be subtle compared to changes in tissue oxygenation induced by tumor hyper-metabolism. Indeed, some groups have observed a decrease of StO_2 in the tumor [25, 26,84–87], whereas others observed no difference [19,21,23,24,40,88] or even an increase [81].

Images of cancer metabolism have been widely utilized in the Positron Emission Tomography (PET) community, wherein breast cancer is frequently characterized by hyper-glucose metabolism measured by increased uptake of ^{18}F-FDG [89,90]. The potential connection between glucose metabolism and oxygen-metabolism of cancer may exist; for example, we observed a positive correlation between the uptake of FDG and *rTHC*, $r\mu_s'$ and *OI* using a subset of the present data [91]. Thus far, however, DOT images of tumor oxygen metabolism have not been achieved due to lack of information about blood flow. In the future, DOT plus blood flow information (either derived by optical means [92,93] or by another technique) hold potential for imaging of tumor metabolism.

The cysts in our DOT images (not shown) exhibited low *rTHC*, $r\mu_s'$ and low StO_2. This observation is in stark contrast to the high *rTHC*, and $r\mu_s'$ of the invasive carcinomas. Generally cysts have been associated with low scattering in DOT images by other groups [24,68,69], since the fluid they enclose is optically thin. Sometimes cysts have exhibited lower *THC* and StO_2 compared to normal tissue as well [26].

The fibroadenoma in our DOT images showed little or no contrast, as was the case for the lobular carcinoma *in situ*. Other groups have reported difficulty detecting fibroadenomas [69]. Note, in our analysis we included lobular carcinoma *in situ* in the benign category to be consistent with such recognition in the clinic [94,95].

E. Core Biopsy Effects

It has been speculated that core biopsy can cause bleeding significant enough to interfere with the hemoglobin-based DOT signal. In some cases, where the bleeding was severe enough to be detected by eye, the corresponding bruise region in the DOT images showed lower blood oxygen level compared to the surrounding tissue, as well as elevated *THC* and scattering. Lower StO_2 in this case may be due to a lack of oxygen supply to the non-circulating blood that has permeated into the extracellular space. However, when these parameters were averaged over the population of each group (i.e. malignant group before and after core biopsy), differences between the pre- and post-biopsy groups were not apparent. This observation indicates that overall variation within each malignant group is more than the variation due to core biopsy effect. In addition, no correlation between the tumor-to-normal ratios of optical parameters and the number of days after biopsy were found (data not shown). This result could change for DOT data measured less than one week after the core biopsy. Clearly, in order to fully understand the effect of core biopsy or fine needle aspiration on the DOT signal, it is desirable to perform a longitudinal study following subjects before and after core biopsy (which is beyond the scope of the present publication).

F. Selection of Optimal Parameters to Differentiate Benign and Malignant Lesions

In order to assess which optical parameters among many are useful for differentiating benign and malignant tumors, we employed an ROC curve analysis for each parameter. Since the influence of core biopsy on our DOT data was determined to be negligible (See Section IV E),

NIH-PA Author Manuscript

NIH-PA Author Manuscript

NIH-PA Author Manuscript

we combined the two groups into one malignant cancer category and compared the malignant group (N=41) with the benign group (N=10). The AUC of *rTHC*, $r\mu_s'$, $rHbO_2$ and *OI* suggested good discriminatory power (> 0.90) to differentiate malignant and benign groups.

ROC curve analysis is important for testing the effectiveness of any diagnostic imaging method. So far, only a few diffuse optics groups have attempted ROC curve analysis. Chance *et al* [25] used a combination of relative *THC* and StO_2 (derived by DOS) of tumors measured with respect to the contralateral side and obtained 95% AUC to discern cancer from normal tissue. In our case, $rStO_2$ did not have much discriminatory power. Furthermore, due to our small number of benign cases, any attempt to combine multiple parameters would result in an overfit of the statistical model. Poplack *et al* [41] achieved 88% AUC for differentiating cancer from normal tissue, and 76% AUC for differentiating malignant cancer from benign lesion distinction using *rTHC* derived from 3D DOT images for a subset of subjects with lesions larger than 6 mm; their AUC decreased when smaller lesions were included in the data set. However, these findings do not represent a final assessment of DOT performance. Each of these papers focused on demonstrations of particular methodology and were not representative of all or even optimized diffuse optical methods. The discrepancy among groups could be a function of methods (e.g. two parameters versus one parameter, localization of tumor with other modalities, etc.) and the variations in the subject groups (e.g. lesion size, percentage of benign and malignant lesions).

G. Future Study Design

A key limitation in our study, as well as those published by other groups, is a small sample size, especially of benign lesions. The lack of statistical significance in benign tumors arises from two effects: (1) A lack of intrinsic lesion-to-normal contrast in some benign lesions, and (2) the small sample size. By averaging over different types of benign lesions, distinct optical signatures of certain lesion types (e.g. cysts) have not been isolated. For future studies, it will be necessary to collect more data (especially benign cases) in order to build stronger predictive model to differentiate benign and malignant lesions. Also, with more data, it should be possible to find the best combination of multiple parameters for differentiation of malignant and benign lesions, and further differentiate lesions types (e.g. ductal carcinoma in situ versus invasive ductal carcinoma, fibroadenoma vs cyst). Furthermore, in the future we can use a large population of lesions without regional averaging (i.e. including the intra-region variability of individual subjects) to develop more advanced analyses that differentiate lesion types and automatically locate lesions in the reconstructed images.

The current instrumentation and analysis scheme is limited because only four lasers were frequency modulated, and because this group did not include the 905 nm laser. Thus it was difficult to directly measure bulk water content. For this reason, we assumed background water and lipid concentrations to be 31% and 57%, respectively, following previous reports in the literature [56–58]. As per continuous wave diffuse optical tomography, we chose not to reconstruct water concentration because approximately half of the patient data was taken without the 905 nm source. Of course, fixing the water concentration can introduce errors in our estimation of *Hb* and HbO_2 concentration. To explore the effects of assumed background water concentration on the relative tumor-to-normal ratios, we performed a full reconstruction on selected data set (N=4) with different assumed water concentration (i.e. at 15, 31, 45 and 60%). These variations in water concentration did not change the overall spatial features of the image (e.g., regions with contrast remained the same). However, extracted *rTHC*, $rStO_2$, $r\mu_s'$, *rHb*, $rHbO_2$ and *OI* did vary somewhat, differing by 4–7%, 3–6%, 5–7%, 7–10%, 6–7%, and 6–14%, respectively, from results with 31% water concentration. These variations are less than inter-subject variability (95% CI) shown in Table IV.

NIH-PA Author Manuscript

NIH-PA Author Manuscript

NIH-PA Author Manuscript

We will address these hardware limitations with "next generation" DOT instruments [96]. This instrument will employ light sources at optimal wavelengths, will add water sensitive wavelengths, and will carry out all measurements in the frequency-domain. This approach will therefore reduce absorption-scattering crosstalk and will permit reconstruction of water and lipid concentration. Finally, such new instrumentation should more readily permit separation of the scattering prefactor A from the scattering power b. In addition, more light source positions will permit denser sampling of small breasts. We will use a sophisticated, automated deformation algorithm [97] to coregister MRI and DOT images taken non-concurrently. Furthermore, the new system will operate in any of sagittal, craniocaudal, or medio-lateral oblique compression, allowing us to better match the clinical imaging geometry and improve our non-concurrent coregistration. The reconstruction algorithm will be improved to further reduce image artifacts and to employ MRI derived anatomical information to constrain our DOT reconstruction algorithms.

V. CONCLUSION

In this paper, we reported diffuse optical tumor-to-normal contrast extracted from three-dimensional reconstructions of 51 breast tumors using our parallel-plate diffuse optical tomography (DOT) system. Elevated regions of total hemoglobin concentration (*THC*) and scattering in malignant cancers in DOT images generally correlated well with tumor regions identified by Magnetic Resonance Imaging. By contrast, cysts exhibited lower scattering than the surrounding tissue, and fibroadenomas showed zero or relatively weaker contrast in *THC* and scattering. The tumor-to-normal ratios in *THC*, HbO_2, scattering and the optical index of the malignant cancer group were statistically significant and different from unity whereas those of benign tumor group were not. These parameters also exhibited high AUC values for distinguishing between malignant and benign lesions. The effect of core biopsy in our malignant tumor group was not statistically significant when DOT measurement was done more than 1 week after core biopsy. Our results suggest that benign and malignant lesions can be distinguished by quantitative three-dimensional DOT. This distinction between benign and malignant lesions is important for efforts to increase sensitivity and specificity of overall breast diagnosis, and for establishing the reliability of the technology for the breast cancer therapy monitoring application.

Acknowledgments

The authors thank Leonid Zubkov for his help on the instrumentation, Han Y. Ban for useful discussion and Yoo Kyung Choe for illustrations. We thank clinical research coordinators who have helped recruitment and measurements: Monika Grosicka-Koptyra, Kathleen McCarthy, and Anisa Nayeem. This research would not have been possible without the generosity of female subjects who participated in our DOT studies. This research was supported by NIH R01-CA75124, R01-EB002109, K99-CA126187, P41-RR002305, NTROI 1U54CA105480 and Army DAMD17-00-1-0408.

APPENDIX

In this section we review the relationship between the measured signal at the CCD and the photon fluence rate at the exit plane of the sample. We also briefly describe the formulation of the objective function used for the inverse problem, including regularization.

Relationship between the fluence rate and the signal detected at the CCD

Consider the schematic of the measurement geometry shown in Figure 7.

A CCD image is obtained for each source position and wavelength. Let $\Phi(\lambda_\omega, \mathbf{r}_s, \mathbf{r})$ denote the fluence rate due to source light originating at $\mathbf{r}_s$ with wavelength λ_ω. The variable $\mathbf{r}$ denotes

NIH-PA Author Manuscript

NIH-PA Author Manuscript

NIH-PA Author Manuscript

position in the sample, including at the exit plane. Furthermore, let $\mathbf{J}(\lambda_\omega, \mathbf{r}_s, \mathbf{r})$ denote the corresponding photon flux at $\mathbf{r}$, and $L(\lambda_\omega, \mathbf{r}_s, \mathbf{r}, \hat{s})$ denote the corresponding photon radiance at $\mathbf{r}$ traveling into the direction $\hat{s}$. In the P_1 approximation of the transport equation [98,99] (i.e. the diffusion approximation), $L(\lambda_\omega, \mathbf{r}_s, \mathbf{r}, \hat{s}) = \frac{1}{4\pi}\Phi(\lambda_\omega, \mathbf{r}_s, \mathbf{r}) + \frac{3}{4\pi}\mathbf{J}(\lambda_\omega, \mathbf{r}_s, \mathbf{r}) \cdot \hat{s}$.

The signal at the CCD plane is detected at a set of discrete points (pixels) of finite size. We denote the detection position on the CCD as $\mathbf{r}_{d,CCD}$. The power, P, reaching one of the CCD pixels centered at position $\mathbf{r}_{d,CCD}$ is explicitly related to $L(\lambda_\omega, \mathbf{r}_s, \mathbf{r}, \hat{s})$, i.e.

$$P(\lambda_\omega, \mathbf{r}_s, \mathbf{r}_{d,\mathrm{CCD}}) = \int_{\text{exit plane}} \int d^2\mathbf{r} \int_{\text{solid angle}} d\Omega(\hat{s})\, L(\lambda_\omega, \mathbf{r}_s, \mathbf{r}, \hat{s})\, T_{\mathrm{Fresnel}}(\hat{s})\, R(\mathbf{r}, \mathbf{r}_{d,\mathrm{CCD}}, \hat{s}). \quad (1)$$

The angular integral extends over whole half-space solid angle, and the spatial integral extends over the entire exit plane. Here $T_{Fresnel}(\hat{s})$ is a transmission factor at the boundary, assumed independent of $\mathbf{r}$ at the exit plane and $\mathbf{r}_{d,CCD}$; it accounts for the relative transmission of light emitted from the same point along different directions into the detection system. $R(\mathbf{r}, \mathbf{r}_{d,CCD}, \hat{s})$ is a response function which gives the probability that light emitted from position $\mathbf{r}$ lands in the pixel centered at $\mathbf{r}_{d,CCD}$. We will assume further that for each $\mathbf{r}_{d,CCD}$ this response function is sharply peaked at $\mathbf{r} = \mathbf{r}_d$, i.e. the response function has a sharp maximum (less than unity) for a small patch of area A centered on $\mathbf{r}_d$ in the exit plane and for $\hat{s}$ within the numerical aperture (NA) of the detection system the response function is zero otherwise. Typically A will be order of 0.1 to 1 mm^2, much larger than the CCD pixel area due to the lens demagnification. The maximum value of this response function also decreases as the radial distance (distance between $\mathbf{r}_d$ and the lens axis) increases, due to beam vignetting [100].

To evaluate Equation 1, we use Fick's law to relate photon fluence rate to photon flux, i.e. $\mathbf{J}(\mathbf{r}) = -\frac{D}{\upsilon}\nabla\Phi(\mathbf{r})$, and we apply the partial current boundary condition for the radiance at the exit plane, i.e. $\Phi(\mathbf{r}) = \frac{1+R_{\mathrm{eff}}}{1-R_{\mathrm{eff}}} 2\frac{D}{\upsilon}\frac{\partial\Phi}{\partial y}$ [101]. Here D is the the photon diffusion coefficient $(D \cong \frac{\upsilon}{3\mu_s'})$, μ_s' is the reduced scattering coefficient, υ is the velocity of light in the medium, and R_{eff} is the effective reflectance at boundary. Evaluating Equation 1 gives

$$P(\lambda_\omega, \mathbf{r}_s, \mathbf{r}_{d,\mathrm{CCD}}) \cong \Phi_m(\lambda_\omega, \mathbf{r}_s, \mathbf{r}_d) \cdot \mathscr{A} \cdot G(\mathbf{r}_d). \quad (2)$$

Here we have assumed that the measured fluence rate, Φ_m, is roughly constant over the patch area A, and we have associated a single $\mathbf{r}_d$ at the exit plane with each $\mathbf{r}_{d,CCD}$. $G(\mathbf{r})$ is a geometric factor that includes the Fresnel factor integral over the system numerical aperture and the Vignetting effect. The corresponding CCD readout, $N(\lambda_\omega, \mathbf{r}_s, \mathbf{r}_{d,CCD}) = \Phi_m(\lambda_\omega, \mathbf{r}_s, \mathbf{r}_d) \cdot A \cdot G(\mathbf{r}_d) \cdot \nu(\lambda_\omega) \cdot g \cdot \Delta t$, where $\nu(\lambda_\omega)$ is the quantum efficiency of detector, Δt is the camera exposure time and g accounts for internal amplifier gains in the detection device. Thus $N(\lambda\omega, \mathbf{r}_s, \mathbf{r}_{d,CCD})$ is proportional to $\Phi_m(\lambda_\omega, \mathbf{r}_s, \mathbf{r}_d)$.

In order to extract tissue optical properties we must compare $\Phi_m(\lambda_\omega, \mathbf{r}_s, \mathbf{r}_d)$ to the calculated fluence rate at the exit plane $\Phi_c(\lambda\omega, \mathbf{r}_s, \mathbf{r}_d)$ based on the optical property distribution in the sample. We compute $\Phi_c(\lambda_\omega, \mathbf{r}_s, \mathbf{r}_d)$ using a finite element method based numerical solver [59], wherein we employ a nonuniform unstructured mesh with higher nodal concentrations at source/detector planes in order to increase the forward model accuracy and suppress image artifacts associated with sources and detectors [60]. We model our reconstruction volume to

NIH-PA Author Manuscript

NIH-PA Author Manuscript

NIH-PA Author Manuscript

mimic the physical boundary system of breast box and also the breast and Intralipid interfaces. The effective reflectance coefficient, R_{eff}, at the boundary is estimated based on the ratio between the refractive index of the sample medium (n) and the outside medium (n_{out}) [102]. At $y = L_y$, we have a glass window (with antireflection coating on the opposite side of the exit plane) which we model as a tissue-glass interface (i.e. $n = 1.4$ and $n_{out} = 1.5$). The $z = 0$ boundary is modeled as a tissue-air boundary (i.e. $n = 1.4$ and $n_{out} = 1.0$). The rest of the black-coated boundaries are modeled as having total absorption ($R_{eff} = 0$). Note that our reconstruction volume in the z direction extends upward to account for the presence of the chest.

Objective function

The objective function, χ^2, is a measure of difference between Φ_m and Φ_c, summed over all the measurements. In our case, we modify a Rytov-type objective function for the multi-spectral method by summing over all source-detector position pairs and all wavelengths. The detailed form of χ^2 is as follows.

$$\chi^2=\frac{1}{2}\sum_{\omega=1}^{N_\lambda}\sum_{s=1}^{N_s}\sum_{d=1}^{N_d}\left(\ln\left(\frac{\Phi_m(\lambda_\omega,\mathbf{r}_s,\mathbf{r}_d)}{\Phi_m^R(\lambda_\omega,\mathbf{r}_s,\mathbf{r}_d)}\frac{\Phi_c^R(\lambda_\omega,\mathbf{r}_s,\mathbf{r}_d)}{\Phi_c(\lambda_\omega,\mathbf{r}_s,\mathbf{r}_d)}\right)\right)^2+Q, \tag{3}$$

$$=\frac{1}{2}\sum_{\omega=1}^{N_\lambda}\sum_{s=1}^{N_s}\sum_{d=1}^{N_d}\left(\ln\left(\frac{N(\lambda_\omega,\mathbf{r}_s,\mathbf{r}_d)}{N^R(\lambda_\omega,\mathbf{r}_s,\mathbf{r}_d)}\frac{\Phi_c^R(\lambda_\omega,\mathbf{r}_s,\mathbf{r}_d)}{\Phi_c(\lambda_\omega,\mathbf{r}_s,\mathbf{r}_d)}\right)\right)^2+Q. \tag{4}$$

Here the image norm $Q=\sum_{k=1}^{N}\gamma(\mathbf{r}_k)\|\mu(\mathbf{r}_k)-\mu^0(\mathbf{r}_k)\|^2$, where μ stands for solution vector (i.e. μ_a and D) and the superscript 0 refers to value of $\mu(\mathbf{r}_k)$ in the previous iteration. In the multi-spectral approach, μ are computed based on the chromophore concentrations, C_l, via the relation $\mu_a(\lambda)=\sum_{l=1}^{L}\varepsilon_l(\lambda)C_l+\mu_a^{bg}(\lambda)$; the scattering factors A, b are related via the relation $\mu_s'(\lambda)=A\lambda^{-b}$. N_λ,N_s,N_d are number of wavelengths, sources and detectors, respectively. The superscript R refers to quantities (i.e. Φ_m, Φ_c or N) derived from the homogeneous Intralipid reference sample. Note that we were able to use our CCD readings, N and N^R, directly in place of Φ_m and Φ_m^R since the proportionality constants are assumed identical between the breast and Intralipid measurements (i.e. the constants cancel one another). The normalization with the Intralipid measurement is important for the integrity of our reconstruction, since it minimizes systematic errors that may be present in our measurement, including the lens Vignetting effect, and source strength fluctuations among different source positions, etc.

$\gamma(\mathbf{r}_k)$ is a spatially variant regularization factor:

$$\begin{aligned}\gamma(\mathbf{r}_k) \quad =\alpha\Bigg[&\exp\left\{-\left(\frac{x-x_{\min}}{L_x}\right)^2\right\}+\exp\left\{-\left(\frac{x-x_{\max}}{L_x}\right)^2\right\}\\&+\exp\left\{-\left(\frac{y-y_{\min}}{L_y/2}\right)^2\right\}+\exp\left\{-\left(\frac{y-y_{\max}}{L_y/2}\right)^2\right\}\\&+\exp\left\{-\left(\frac{z-z_{\min}}{L_z}\right)^2\right\}+\exp\left\{-\left(\frac{z-z_{\max}}{L_z}\right)^2\right\}\Bigg].\end{aligned} \tag{5}$$

Here α is the regularization parameter, and L_x,L_y,L_z are the dimensions of the sample box. x_{min}, y_{min}, z_{min} and x_{max}, y_{max}, z_{max} are minimum and maximum coordinates of the sample box

NIH-PA Author Manuscript

NIH-PA Author Manuscript

NIH-PA Author Manuscript

respectively. Note that *y* is the axis perpendicular to the source and detection planes. For L-curve analysis, we varied α as described in the text (Section 2.3). We use the nonlinear conjugate gradient method to minimize χ^2, computing the search direction based on the gradient of χ^2 [61]. This method does not require a matrix inversion for computing search directions. Therefore, it is especially useful for systems with large number of source-detector pairs and large reconstruction domains wherein building and inverting the Jacobian matrix can be computationally difficult and even impossible due to memory limitations.

References

1. American Cancer Society, Statistics for 2007 : Cancer Facts & Figures 2007. http://www.cancer.org/docroot/STT/stt 0.asp
2. Kerlikowske K, Barclay J, Grady D, Sickles EA, Ernster V. Comparison of risk factors for ductal carcinoma in situ and invasive breast cancer. J. Natl. Cancer Inst 1997;89(1):76–82. [PubMed: 8978410]
3. Murphy IG, Dillon MF, O'Doherty A, McDermott EW, Kelly G, O'Higgins N, Hill ADK. Analysis of patients with false negative mammography and symptomatic breast carcinoma. J. Surg. Oncol 2007;96:457–463. [PubMed: 17929256]
4. Fletcher SW. Breast cancer screening among women in their forties: an overview of the issues. J. Natl. Cancer Inst. Monogr 1997;22:5–9. [PubMed: 9709267]
5. Elmore JG, Barton MB, Moceri VM, Polk S, Arena PJ, Fletcher SW. Ten-year risk of false positive screening mammograms and clinical breast examinations. New Engl. J. Med 1998;338:1089–1096. [PubMed: 9545356]
6. Goergen SK, Evans J, Cohen GPB, MacMillan JH. Characteristics of breast carcinomas missed by screening radiologists. Radiology 1997;204:131–135. [PubMed: 9205234]
7. Birdwell RL, Ikeda DM, O'Shaughnessy KF, Sickles EA. Mammographic characteristics of 115 missed cancers later detected with screening mammography and the potential utility of computer-aided detection. Radiology 2001;219(1):192–202. [PubMed: 11274556]
8. Wang J, Shih TT, Hsu JC, Li YW. The evaluation of false negative mammography from malignant and benign breast lesions. J. Clin. Imaging 2000;24:96–103.
9. Franceschini MA, Moesta KT, Fantini S, Gaida G, Gratton E, Jess H, Mantulin WW, Seeber M, Schlag PM, Kaschke M. Frequency-domain techniques enhance optical mammography: Initial clinical results. Proc. Natl. Acad. Sci. U. S. A 1997;94:6468–6473. [PubMed: 9177241]
10. Colak SB, van der Mark MB, Hooft GW, Hoogenraad JH, van der Linden ES, Kuijpers FA. Clinical optical tomography and NIR spectroscopy for breast cancer detection. IEEE J. Quantum Electron 1999;5(4):1143–1158.
11. Ntziachristos V, Yodh AG, Schnall M, Chance B. Concurrent MRI and diffuse optical tomography of breast after indocyanine green enhancement. Proc. Natl. Acad. Sci. U. S. A 2000;97:2767–2772. [PubMed: 10706610]
12. Tromberg BJ, Shah N, Lanning R, Cerussi A, Espinoza J, Pham T, Svaasand L, Butler J. Non-invasive in vivo characterization of breast tumors using photon migration spectroscopy. Neoplasia 2000;2:26–40. [PubMed: 10933066]
13. Pogue BW, Poplack SP, McBride TO, Wells WA, Osterman KS, Osterberg UL, Paulsen KD. Quantitative hemoglobin tomography with diffuse near-infrared spectroscopy: Pilot results in the breast. Radiology 2001;218:261–266. [PubMed: 11152812]
14. Jiang H, Xu Y, Ifitimia N, Eggert J, Klove K, Baron L, Fajardo L. Three-dimensional optical tomographic imaging of breast in a human subject. IEEE Trans. Med. Imaging 2001;20:1334–1340. [PubMed: 11811833]
15. Dehghani H, Pogue BW, Jiang SD, Brooksby B, Paulsen KD. Three-dimensional optical tomography: resolution in small-object imaging. Appl. Opt 2003;42:3117–3128. [PubMed: 12790463]
16. Li A, Miller EL, Kilmer ME, Brukilacchio TJ, Chaves T, Stott J, Zhang Q, Wu T, Chorlton M, Moore RH, Kopans DB, Boas DA. Tomographic optical breast imaging guided by three-dimensional mammography. Appl. Opt 2003;42:5181–5190. [PubMed: 12962399]

NIH-PA Author Manuscript

NIH-PA Author Manuscript

NIH-PA Author Manuscript

17. Zhu QI, Huang MM, Chen NG, Zarfos K, Jagjivan B, Kane M, Hedge P, Kurtzman SH. Ultrasound-guided optical tomographic imaging of malignant and benign breast lesions: Initial clinical results of 19 cases. Neoplasia 2003;5:379–388. [PubMed: 14670175]

18. Jakubowski DB, Cerussi AE, Bevilacqua F, Shah N, Hsiang D, Butler J, Tromberg BJ. Monitoring neoadjuvant chemotherapy in breast cancer using quantitative diffuse optical spectroscopy: a case study. J. Biomed. Opt 2004;9:230–238. [PubMed: 14715078]

19. Choe R, Corlu A, Lee K, Durduran T, Konecky SD, Grosicka-Koptyra M, Arridge SR, Czerniecki BJ, Fraker DL, DeMichele A, Chance B, Rosen MA, Yodh AG. Diffuse optical tomography of breast cancer during neoadjuvant chemotherapy: a case study with comparison to MRI. Med. Phys 2005;32 (4):1128–1139. [PubMed: 15895597]

20. Schmitz CH, Klemer DP, Hardin R, Katz MS, Pei Y, Graber HL, Levin MB, Levina RD, Fraco NA, Solomon WB, Barbour RL. Design and implementation of dynamic near-infrared optical tomographic imaging instrumentation for simultaneous dual-breast measurements. Appl. Opt 2005;44:2140–2153. [PubMed: 15835360]

21. Intes X, Djeziri S, Ichalalene Z, Mincu N, Wang Y, St-Jean P, Lesage F, Hall D, Boas D, Polyzos M, Fleiszer D, Mesurolle B. Time-Domain optical mammography SoftScan: Initial results. Acad. Radiol 2005;12:934–947. [PubMed: 16023382]

22. Grosenick D, Moesta KT, Möller M, Mucke J, Wabnitz H, Gebauer B, Stroszczynski C, Wassermann B, Schlag PM, Rinneberg H. Time-domain scanning optical mammography: I. Recording and assessment of mammograms of 154 patients. Phys. Med. Biol 2005;50(11):2429–2450. [PubMed: 15901947]

23. Grosenick D, Wabnitz H, Moesta KT, Mucke J, Schlag PM, Rinneberg H. Time-domain scanning optical mammography: II. Optical properties and tissue parameters of 87 carcinomas. Phys. Med. Biol 2005;50(11):2451–2468. [PubMed: 15901948]

24. Spinelli L, Torricelli A, Pifferi A, Taroni P, Danesini G, Cubeddu R. Characterization of female breast lesions from multi-wavelength time-resolved optical mammography. Phys. Med. Biol 2005;50(11): 2489–2502. [PubMed: 15901950]

25. Chance B, Nioka S, Zhang J, Conant EF, Hwang E, Briest S, Orel SG, Schnall MD, Czerniecki BJ. Breast cancer detection based on incremental biochemical and physiological properties of breast cancers: A six-year, two-site study. Acad. Radiol 2005;12:925–933. [PubMed: 16023383]

26. Enfield LC, Gibson AP, Everdell NL, Delpy DT, Schweiger M, Arridge SR, Richardson C, Keshtgar M, Douek M, Hebden JC. Three-dimensional time-resolved optical mammography of the uncompressed breast. Appl. Opt 2007;46:3628–3638. [PubMed: 17514325]

27. Zhu Q, Kurtzma SH, Hegde P, Tannenbaum S, Kane M, Huang M, Chen NG, Jagjivan B, Zarfos K. Utilizing optical tomography with ultrasound localization to image heterogeneous hemoglobin distribution in large breast cancers. Neoplasia 2005;7(3):263–270. [PubMed: 15799826]

28. Srinivasan S, Pogue BW, Brooksby B, Jiang S, Dehghani H, Kogel C, Wells WA, Poplack SP, Paulsen KD. Near-Infrared characterization of breast tumors in vivo using spectrally-constrained reconstruction. Tech. Cancer Res. Treat 2005;4:513–526.

29. Li C, Grobmyer SR, Massol N, X L, Zhang Q, Chen L, Fajardo LL, Jiang H. Noninvasive in vivo tomographic optical imaging of cellular morphology in the breast: Possible convergence of microscopic pathology and macroscopic radiology. Med. Phys 2008;35:2493–2501. [PubMed: 18649482]

30. Folkman J, Watson K, Ingber D, Hanahan D. Induction of angiogenesis during the transition from hyperplasia to neoplasia. Nature 1989;339:58–61. [PubMed: 2469964]

31. Vaupel P, Thews O, Kelleher DK, Hoeckel M. Current status of knowledge and critical issues in tumor oxygenation. Results from 25 years research in tumor pathophysiology. Adv. Exp. Med. Biol 1998;454:591–602. [PubMed: 9889939]

32. Vaupel P, Schlenger K, Knoop C, Hockel M. Oxygenation of human tumors: evaluation of tissue oxygen distribution in breast cancers by computerized O_2 tension measurements. Cancer Res 1991;51 (12):3316–3322. [PubMed: 2040005]

33. Weidner N, Folkman J, Pozza F, Bevilacqua P, Allred DC, Moore DH, Meli S, Gasparini G. Tumor angiogenesis: A new significant and independent prognostic indicator in early-stage breast carcinoma. J. Natl. Cancer Inst 1992;84:1875–1887. [PubMed: 1281237]

NIH-PA Author Manuscript

NIH-PA Author Manuscript

NIH-PA Author Manuscript

34. Thomsen S, Tatman D. Physiological and pathological factors of human breast disease that can influence optical diagnosis. Ann. N. Y. Acad. Sci 1998;838:171–193. [PubMed: 9511805]
35. Mourant JR, Freyer JP, Hielscher AH, Eick AA, Shen D, Johnson TM. Mechanisms of light scattering from biological cells relevant to noninvasive optical-tissue diagnosis. Appl. Opt 1998;37:3586–3593. [PubMed: 18273328]
36. Hebden JC, Yates TD, Gibson A, Everdell N, Arridge SR, Chicken DW, Douek M, Keshtgar MRS. Monitoring recovery after laser surgery of the breast with optical tomography: a case study. Appl. Opt 2005;44(10):1898–1904. [PubMed: 15813526]
37. Shah N, Gibbs J, Wolverton D, Cerussi A, Hylton N, Tromberg BJ. Combined diffuse optical spectroscopy and contrast-enhanced magnetic resonance imaging for monitoring breast cancer neoadjuvant chemotherapy: a case study. J. Biomed. Opt 2005;10051,503
38. Cerussi A, Hsiang D, Shah N, Mehta R, Durkin A, Butler J, Tromberg BJ. Predicting response to breast cancer neoadjuvant chemotherapy using diffuse optical spectroscopy. Proc. Natl. Acad. Sci. U. S. A 2007;104:4014–4019. [PubMed: 17360469]
39. Zhu Q, Tannenbaum S, Hegde P, Kane M, Xu C, Kurtzman SH. Noninvasive monitoring of breast cancer during neoadjuvant chemotherapy using optical tomography with ultrasound localization. Neoplasia 2008;10:1028–1040. [PubMed: 18813360]
40. Cerussi A, Shah N, Hsiang D, Durkin A, Butler J, Tromberg BJ. In vivo absorption, scattering, and physiologic properties of 58 malignant breast tumors determined by broadband diffuse optical spectroscopy. J. Biomed. Opt 2006;11044,005
41. Poplack SP, Tosteson TD, Wells WA, Pogue BW, Meaney PM, Hartov A, Kogel CA, Soho SK, Gibson JJ, Paulsen KD. Electromagnetic Breast Imaging: Results of a Pilot Study in Women with Abnormal Mammograms. Radiology 2007;243(2):350–359. [PubMed: 17400760]
42. Leff DR, Warren OJ, Enfield LC, Gibson A, Athanasiou T, Patten DK, Hebden J, Yang GZ, Darzi A. Diffuse optical imaging of the healthy and diseased breast: A systematic review. Breast Cancer Res. Treat 2008;108:9–22. [PubMed: 17468951]
43. Konecky SD, Panasyuk GY, Lee K, Markel VA, Yodh AG, Schotland JC. Imaging complex structures with diffuse light. Opt. Express 2008;16:5048–5060. [PubMed: 18542605]
44. Culver JP, Choe R, Holboke MJ, Zubkov L, Durduran T, Slemp A, Ntziachristos V, Chance B, Yodh AG. Three-dimensional diffuse optical tomography in the parallel plane transmission geometry: Evaluation of a hybrid frequency domain/continuous wave clinical system for breast imaging. Med. Phys 2003;30:235–247. [PubMed: 12607841]
45. Corlu A, Durduran T, Choe R, Schweiger M, Hillman EMC, Arridge SR, Yodh AG. Uniqueness and wavelength optimization in continuous-wave multispectral diffuse optical tomography. Opt. Lett 2003;28:2339–2341. [PubMed: 14680175]
46. Corlu A, Choe R, Durduran T, Lee K, Schweiger M, Arridge SR, Hillman EMC, Yodh AG. Diffuse optical tomography with spectral constraints and wavelength optimization. Appl. Opt 2005;44(11): 2082–2093. [PubMed: 15835357]
47. Yang YS, Liu HL, Li XD, Chance B. Low-cost frequency-domain photon migration instrument for tissue spectroscopy, oximetry, and imaging. Opt. Eng 1997;36(5):1562–1569.
48. Yates T, Hebden JC, Gibson A, Everdell N, Arridge SR, Douek M. Optical tomography of the breast using a multi-channel time-resolved imager. Phys. Med. Biol 2005;50(11):2503–2518. [PubMed: 15901951]
49. Prahl, S. Optical Properties Spectra. compiled data published on-line at http://omlc.ogi.edu/spectra/index.html
50. Ishimaru, A. Wave Propagation and Scattering in Random Media. San Diego: Academic Press, Inc.; 1978.
51. Furutsu K. On the diffusion equation derived from the space-time transport equation. J. Opt. Soc. Am. A 1980;70:360–366.
52. Groenhuis RAJ, Ferwerda HA, Ten Bosch JJ. Scattering and absorption of turbid materials determined from reflection measurements. I. Theory. Appl. Opt 1983;22:2456–2462. [PubMed: 18196156]
53. Mourant JR, Fuselier T, Boyer J, Johnson TM, Bigio IJ. Predictions and measurements of scattering and absorption over broad wavelength ranges in tissue phantoms. Appl. Opt 1997;39:949–957. [PubMed: 18250760]

NIH-PA Author Manuscript

NIH-PA Author Manuscript

NIH-PA Author Manuscript

54. Bevilacqua F, Berger AJ, Cerussi AE, Jakubowski D, Tromberg BJ. Broadband absorption spectroscopy in turbid media by combined frequency-domain and steady-state methods. Appl. Opt 2000;39:6498–6507. [PubMed: 18354663]
55. Durduran T, Choe R, Culver JP, Zubkov L, Holboke MJ, Giammarco J, Chance B, Yodh AG. Bulk optical properties of healthy female breast tissue. Phys. Med. Biol 2002;47:2847–2861. [PubMed: 12222850]
56. Woodard HQ, White DR. The composition of body tissues. Br. J. Radiol 1986;59:1209–1219. [PubMed: 3801800]
57. White DR, Woodard HQ, Hammond SM. Average soft-tissue and bone models for use in radiation dosimetry. Br. J. Radiol 1987;60:907–913. [PubMed: 3664185]
58. Lee NA, Rusinek H, Weinreb JC, Chandra R, Singer RC, Newstead GM. Fatty and fibroglandular tissue volumes in the breasts of women 20–83 years old: comparison of x-ray mammography and computer-assisted MR imaging. Am. J. Radiol 1997;168:501–506.
59. Arridge SR, Schweiger M. Photon-measurement density functions. Part 2: Finiteelement-method calculations. Appl. Opt 1995;34(34):8026–8036.
60. Lee, K.; Choe, R.; Corlu, A.; Konecky, SD.; Durduran, T.; Yodh, AG. Artifact reduction in CW transmission diffuse optical tomography; OSA Biomedical Topical Meetings; Washington, DC: The Optical Society of America; 2004.
61. Arridge SR, Schweiger M. A gradient-based optimisation scheme for optical tomography. Opt. Express 1998;2(6):213–226. [PubMed: 19377605]
62. Pogue BW, McBride TO, Prewitt J, Osterberg UL, Paulsen KD. Spatially variant regularization improves diffuse optical tomography. Appl. Opt 1999;38:2950–2961. [PubMed: 18319877]
63. Kaufman L, Neumaier A. PET regularization by envelope guided conjugate gradients. IEEE Trans. Med. Imaging 1996;15:385–389. [PubMed: 18215919]
64. Corlu, A.; Choe, R.; Durduran, T.; Lee, K.; Konecky, SD.; Yodh, AG. Regularization of diffuse optical tomography images by envelope guided conjugate gradients; Biomedical Topical Meetings, ThD4; Washington, DC: The Optical Society of America; 2004.
65. R. D. C. Team. R: A language and environment for statistical computing. Vienna, Austria: R Foundation for Statistical Computing; 2007.
66. Pinheiro, JC.; Bates, DM. Mixed-Effects Models in S and S-PLUS. New York, NY: Springer; 2000.
67. Sing T, Sander O, Beerenwinkel N, Lengauer T. ROCR: visualizing classifier performance in R. Bioinformatics 2005;21:3940–3941. [PubMed: 16096348]
68. Gu XJ, Zhang QZ, Bartlett M, Schutz L, Fajardo LL, Jiang HB. Differentiation of cysts from solid tumors in the breast with diffuse optical tomography. Acad. Radiol 2004;11:53–60. [PubMed: 14746402]
69. Taroni P, Torricelli A, Spinelli L, Pifferi A, Arpaia F, Danesini G, Cubeddu R. Time-resolved optical mammography between 637 and 985 nm: clinical study on the detection and identification of breast lesions. Phys. Med. Biol 2005;50(11):2469–2488. [PubMed: 15901949]
70. Ntziachristos V, Yodh AG, Schnall MD, Chance B. MRI-guided diffuse optical spectroscopy of malignant and benign breast lesions. Neoplasia 2002;4:347–354. [PubMed: 12082551]
71. Brooksby B, Pogue BW, Jiang S, Dehghani H, Srinivasan S, Kogel C, Tosteson TD, Weaver J, Poplack SP, Paulsen KD. Imaging breast adipose and fibroglandular tissue molecular signatures by using hybrid MRI-guided near-infrared spectral tomography. Proc. Natl. Acad. Sci 2006;103:8828–8833. [PubMed: 16731633]
72. Carpenter CM, Pogue BW, Jiang S, Dehghani H, Wang X, Paulsen KD, Wells WA, Forero J, Kogel C, Weaver JB, Poplack SP, Kaufman PA. Image-guided optical spectroscopy provides molecular-specific information in vivo: MRI-guided spectroscopy of breast cancer hemoglobin, water, and scatterer size. Optics Letters 2007;32(8):933–935. [PubMed: 17375158]
73. Zhang Q, Brukilacchio TJ, Li A, Stott JJ, Chaves T, Hillman E, Wu T, Chorlton A, Rafferty E, Moore RH, Kopans DB, Boas DA. Coregistered tomographic x-ray and optical breast imaging: initial results. J. Biomed. Opt 2005;10(2)024,033
74. Boverman G, Fang Q, Carp SA, Miller EL, Brooks DH, Selb J, Moore RH, Kopans DB, Boas DA. Spatio-temporal imaging of the hemoglobin in the compressed breast with diffuse optical tomography. Phys. Med. Biol 2007;52(12):3619–3641. [PubMed: 17664563]

NIH-PA Author Manuscript

NIH-PA Author Manuscript

NIH-PA Author Manuscript

75. Tofts PS, Berkowitz B, Schnall MD. Quantitative analysis of dynamic Gd-DTPA enhancement in breast tumors using a permeability model. Magn. Reson. Med 1995;33:564–568. [PubMed: 7776889]
76. Perini R, Choe R, Yodh AG, Sehgal C, Divgi C, Rosen MA. Non-invasive Assessment of Tumor Neovasculature: Techniques and Clinical Applications. Cancer and Metastasis Reviews 2008;27:615–630. [PubMed: 18506398]
77. Srinivasan S, Pogue BW, Jiang SD, Dehghani H, Kogel C, Soho S, Gibson JJ, Tosteson TD, Poplack SP, Paulsen KD. Interpreting hemoglobin and water concentration, oxygen saturation, and scattering measured in vivo by near-infrared breast tomography. Proc. Natl. Acad. Sci. U. S. A 2003;100:12,349–12,354.
78. Spinelli L, Torricelli A, Pifferi A, Taroni P, Danesini GM, Cubeddu R. Bulk optical properties and tissue components in the female breast from multiwavelength time-resolved optical mammography. J. Biomed. Opt 2004;9:1137–1142. [PubMed: 15568933]
79. Folkman J, Beckner K. Angiogenesis imaging. Acad. Radiol 2000;7:783–785. [PubMed: 11048875]
80. Pogue BW, Poplack SP, McBride TO, Wells WA, Osterman KS, Osterberg UL. Hemoglobin imaging of breast tumors with near-infrared tomography. Radiology 2000;214609-609
81. Dehghani H, Pogue BW, Poplack SP, Paulsen KD. Multiwavelength three-dimensional near-infrared tomography of the breast: initial simulation, phantom, and clinical results. Appl. Opt 2003;42:135–145. [PubMed: 12518832]
82. Jiang HB, Iftimia NV, Xu Y, Eggert JA, Fajardo LL, Klove KL. Near-infrared optical imaging of the breast with model-based reconstruction. Acad. Radiol 2002;9:186–194. [PubMed: 11918371]
83. Zhu Q, Chen N, Kurtzman SH. Imaging tumor angiogenesis by use of combined near-infrared diffusive light and ultrasound. Opt. Lett 2003;28:337–339. [PubMed: 12659436]
84. Fantini S, Walker SA, Franceschini MA, Kaschke M, Schlag PM, Moesta KT. Assessment of the size, position, and optical properties of breast tumors in vivo by noninvasive optical methods. Appl. Opt 1998;37:1982–1989. [PubMed: 18273118]
85. Chernomordik V, Hattery DW, Grosenick D, Wabnitz H, Rinneberg H, Moesta KT, Schlag PM, Gandjbakhche A. Quantification of optical properties of a breast tumor using random walk theory. J. Biomed. Opt 2002;7:80–87. [PubMed: 11818015]
86. Heffer E, Pera V, Schutz O, Siebold H, Fantini S. Near-infrared imaging of the human breast: complementing hemoglobin concentration maps with oxygenation images. J. Biomed. Opt 2004;9:1152–1160. [PubMed: 15568935]
87. Srinivasan S, Pogue BW, Carpenter C, Jiang S, Wells WA, Poplack SP, Kaufman PA, Paulsen KD. Developments in quantitative oxygen-saturation imaging of breast tissue in vivo using multispectral near-infrared tomography. Antioxidants & Redox Signaling 2007;9:1143–1156. [PubMed: 17627478]
88. McBride TO, Pogue BW, Poplack S, Soho S, Wells WA, Jiang SD, Osterberg UL, Paulsen KD. Multispectral near-infrared tomography: a case study in compensating for water and lipid content in hemoglobin imaging of the breast. J. Biomed. Opt 2002;7:72–79. [PubMed: 11818014]
89. Wahl RL. Overview of the current status of PET in breast cancer imaging. Q. J. Nucl. Med 1998;42:1–7. [PubMed: 9646639]
90. Bombardieri E, Crippa F. PET imaging in breast cancer. Q. J. Nucl. Med 2001;45(3):245–255. [PubMed: 11788817]
91. Konecky SD, Choe R, Corlu A, Lee K, Wiener R, Srinivas SM, Saffer JR, Freifelder R, Karp JS, Hajjioui N, Azar F, Yodh AG. Comparison of diffuse optical tomography of human breast with whole-body and breast-only positron emission tomography. Med. Phys 2008;35:446–455. [PubMed: 18383664]
92. Durduran T, Choe R, Yu G, Zhou C, Tchou JC, Czerniecki BJ, Yodh AG. Diffuse optical measurement of blood flow in breast tumors. Opt. Lett 2005;30:2915–2917. [PubMed: 16279468]
93. Zhou C, Choe R, Shah N, Durduran T, Yu G, Durkin A, Hsiang D, Mehta R, Butler J, Cerussi A, Tromberg BJ, Yodh AG. Diffuse optical monitoring of blood flow and oxygenation in human breast cancer during early stages of neoadjuvant chemotherapy. J. Biomed. Opt 2007;12051,903
94. Rosen, PP. Rosen's Breast Pathology. Philadelphia: Lippincott Williams & Wilkins; 1997.
95. Silva, OE.; Zurrida, S., editors. Breast Cancer: A Practical Guide. Amsterdam: Elsevier; 2000.

NIH-PA Author Manuscript

NIH-PA Author Manuscript

NIH-PA Author Manuscript

96. Lee, K.; Konecky, SD.; Choe, R.; Ban, HY.; Colu, A.; Durduran, T.; Yodh, AG. Transmission RF diffuse optical tomography instrument for human breast imaging; European Conferences on Biomedical Optics, OSA; Germany: Munich; 2007.

97. Azar FS, Lee K, Khamene A, Choe R, Corlu A, Konecky SD, Sauer F, Yodh AG. Standardized platform for coregistration of non-concurrent diffuse optical and magnetic resonance breast images obtained in different geometries. J. Biomed. Opt 2007;12051,902

98. Davison, B.; Sykes, JB. Neutron Transport Theory. London: Oxford University Press; 1957.

99. Case, MC.; Zweifel, PF. Linear Transport Theory. New York: Addison-Wesley; 1967.

100. Ray, SF. Applied photographic optics. Oxford: Focal Press; 2002.

101. Haskell RC, Svaasand LO, Tsay T, Feng T, McAdams MS, Tromberg BJ. Boundary Conditions for the diffusion equation in radiative transfer. J. Opt. Soc. Am. A 1994;11:2727–2741.

102. Egan, WG.; Hilgeman, TW. Optical Properties of Inhomogeneous Materials. New York: Academic; 1979.

NIH-PA Author Manuscript
NIH-PA Author Manuscript
NIH-PA Author Manuscript

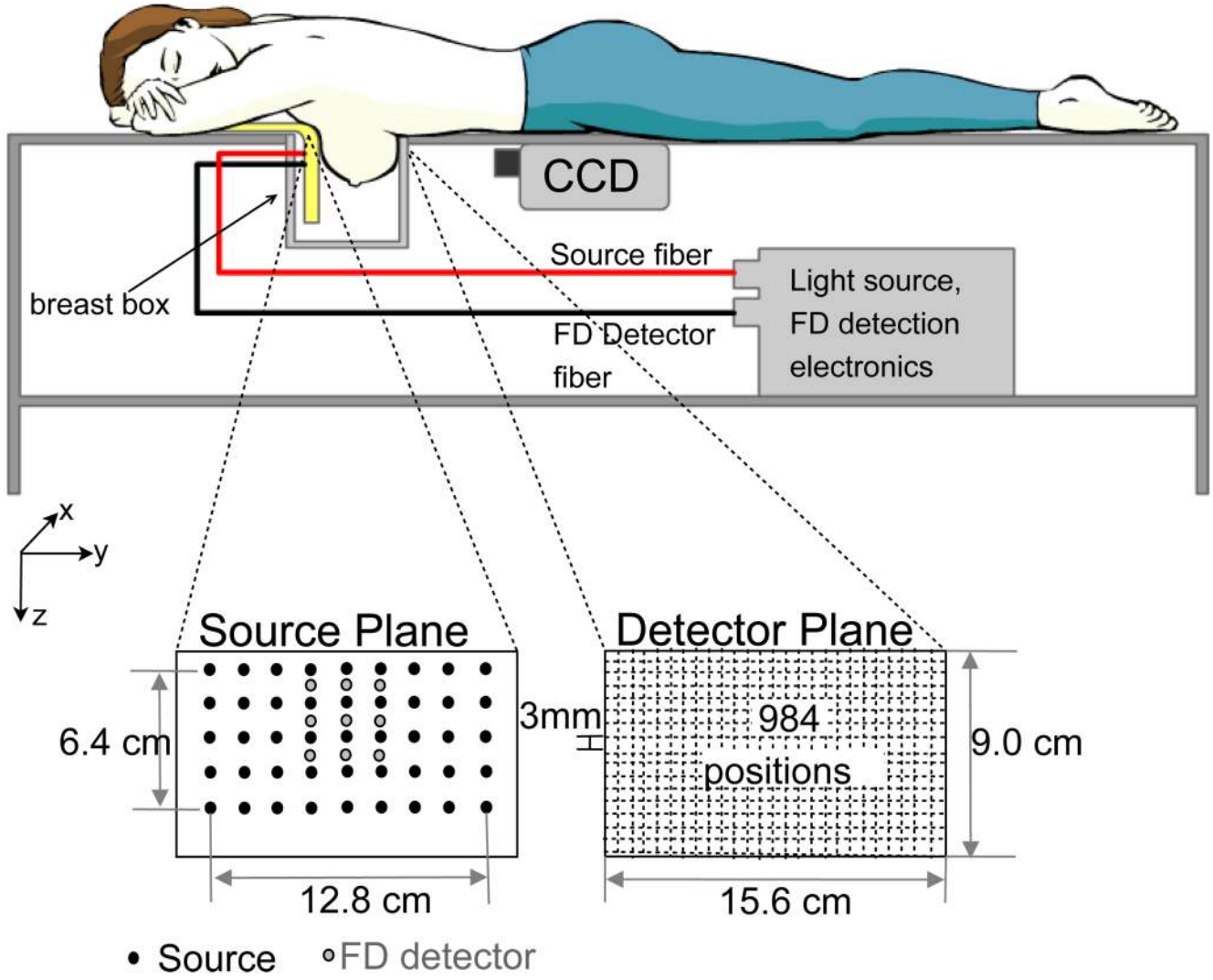

FIG. 1.

Schematic of the parallel plate diffuse optical tomography instrument. A female subject lies in prone position on a bed with her breasts inside the breast box filled with a matching fluid. Continuous-wave transmission and frequency-domain remission measurements are performed simultaneously by a CCD camera and nine Avalanche Photodiodes connected by fibers on the source plate for 45 source positions at multiple wavelengths.

NIH-PA Author Manuscript

NIH-PA Author Manuscript

NIH-PA Author Manuscript

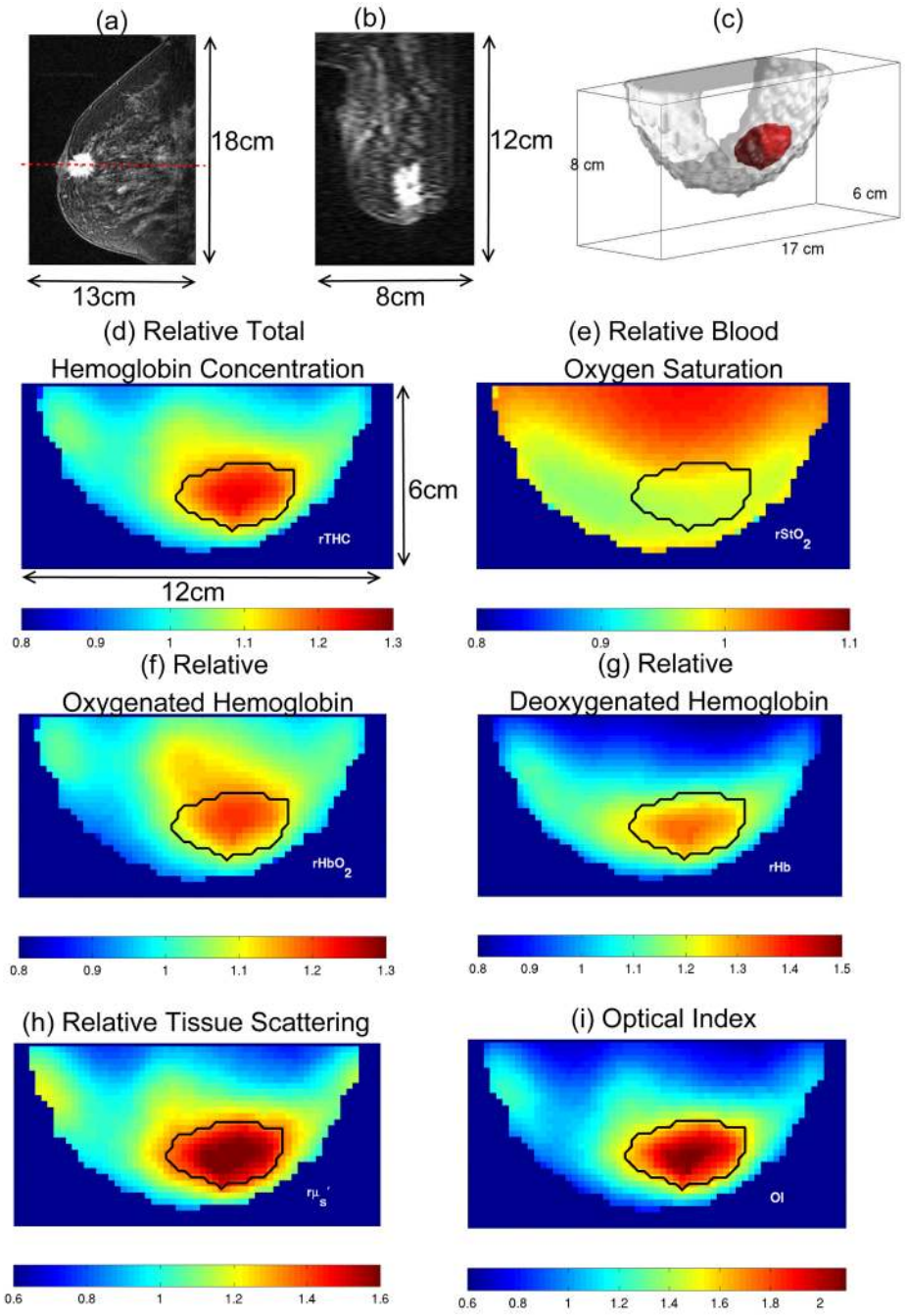

FIG. 2.

MR image and DOT image of a 53-yr-old woman with a 2.2cm invasive ductal carcinoma in her right breast. (a) is the sagittal dynamic-contrast-enhanced (DCE) MRI containing the tumor center, (b) is the axial DCE MRI slice along the red horizontal line in (a), oriented in caudal-cranial view. Enhancement of gadolinium uptake in MRI indicates the malignancy. (c) depicts the tumor region (in red) determined based on optical data with the guidance of MRI and the breast outline (in pink) in three-dimensional space. DOT images of (d) relative total hemoglobin concentration *rTHC*, (e) relative blood oxygen saturation $rStO_2$, (f) relative oxygenated hemoglobin concentration $rHbO_2$, (g) relative deoxygenated hemoglobin

concentration *rHb*, (h) relative tissue scattering $r\mu_s'$ at 786 nm and (i) optical index *OI* are shown in caudal-cranial view with a black solid line indicating the region identified as tumor using a region-growing algorithm. High tumor-to-normal contrast in *rTHC*, $rHbO_2$, *rHb*, $r\mu_s'$ and *OI* are visible within the region.

NIH-PA Author Manuscript
NIH-PA Author Manuscript
NIH-PA Author Manuscript

NIH-PA Author Manuscript

NIH-PA Author Manuscript

NIH-PA Author Manuscript

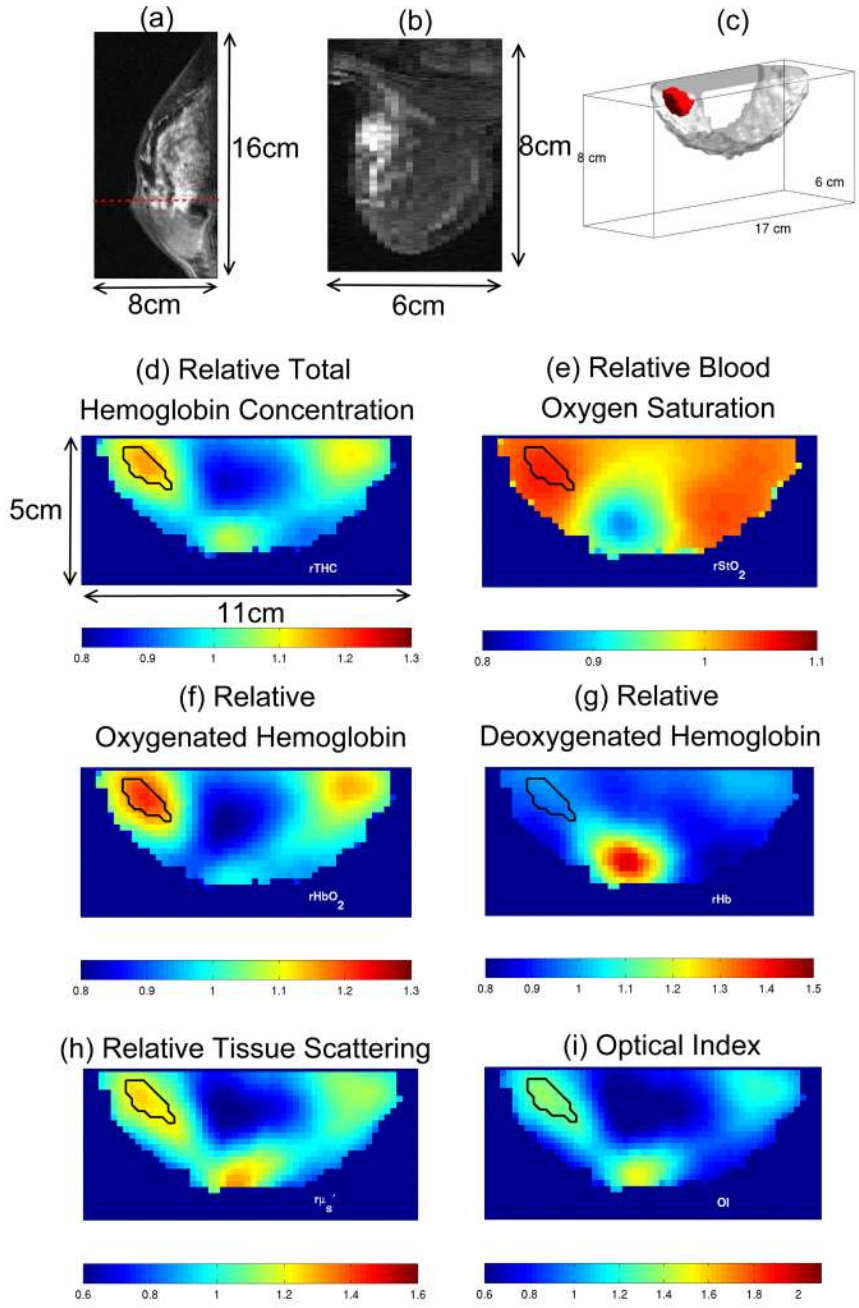

FIG. 3.

MR image and DOT image of a 39-yr-old woman with ductal and lobular carcinoma *in situ* spanning 3 – 5 cm in her left breast. The axial DCE-MR image shows enhancement at the lesion. The black solid line indicates tumor region determined by a region growing algorithm based on this information from MRI. DOT images show elevated $rTHC$, $rHbO_2$, $r\mu_s'$ and OI in tumor region compared to the surrounding tissue.

NIH-PA Author Manuscript

NIH-PA Author Manuscript

NIH-PA Author Manuscript

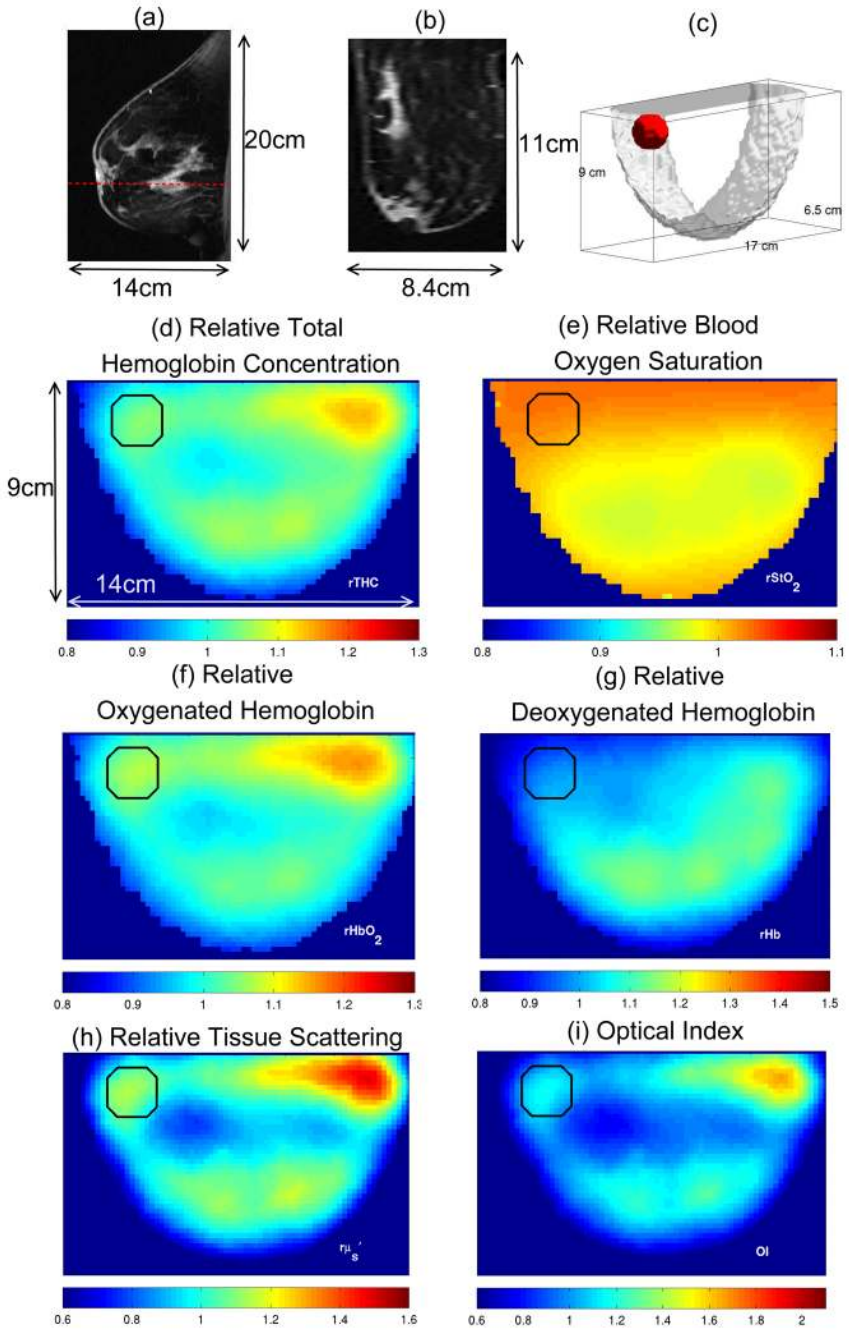

FIG. 4.

MR image and DOT image of a 51-yr-old woman with a 5 mm fibroadenoma in her left breast. The DCE-MR image shows an asymmetric density exhibiting some enhancement in lower outer quadrant. Since the optical contrast was not apparent, a spherical region was assigned as a benign lesion in DOT images (black solid line) based on the extent of gadolinium enhancement in DCE-MR image. Tumor-to-normal contrast in all parameters and *OI* are similar to that of surrounding tissue.

NIH-PA Author Manuscript

NIH-PA Author Manuscript

NIH-PA Author Manuscript

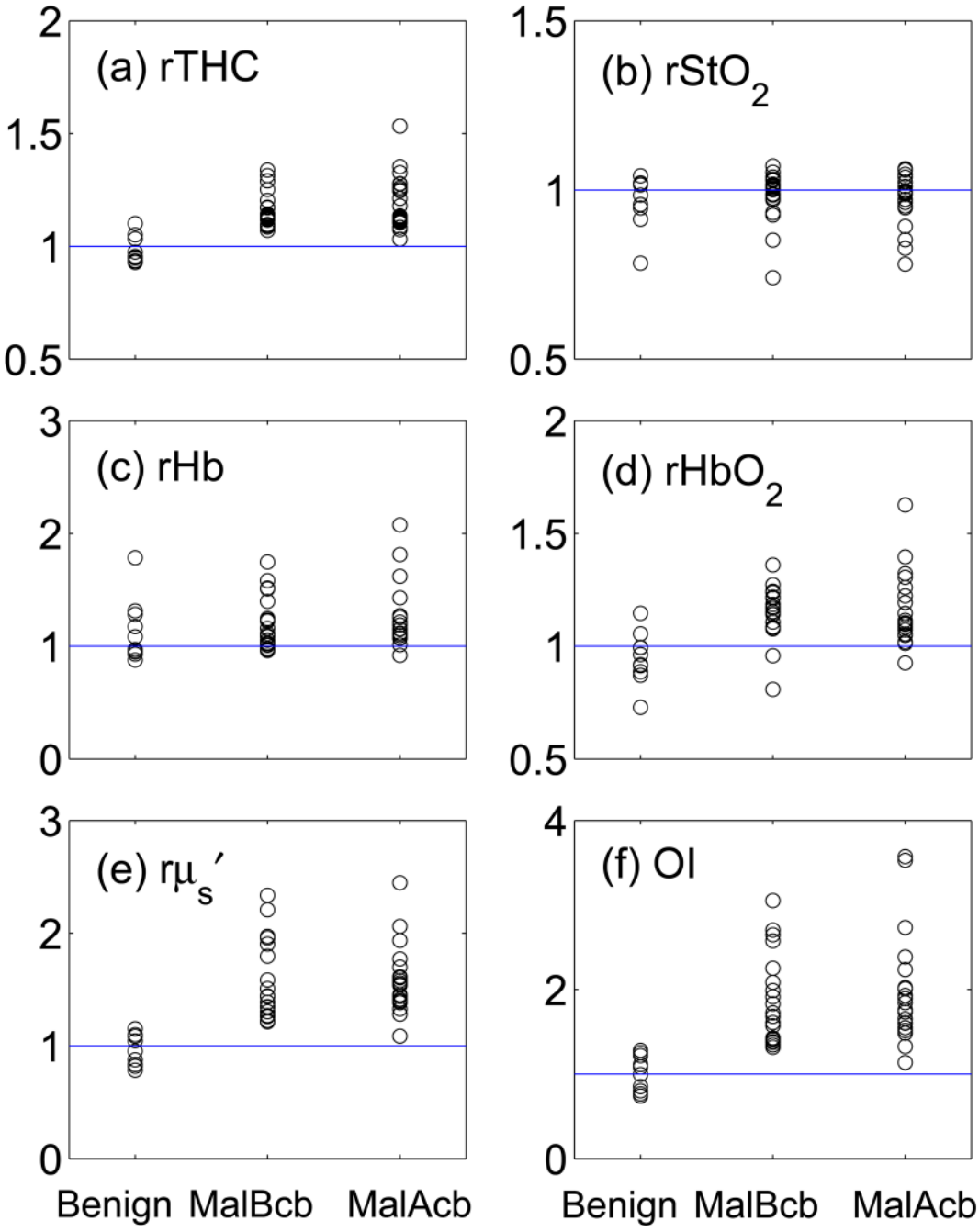

FIG. 5.

rTHC, $rStO_2$, $r\mu_s'$, *rHb*, $rHbO_2$ and *OI* of all 51 lesions. Lesions are separated into three groups: benign lesions, malignant lesions measured before core-biopsy (malBcb), and malignant lesions measured after core-biopsy (malAcb).

NIH-PA Author Manuscript

NIH-PA Author Manuscript

NIH-PA Author Manuscript

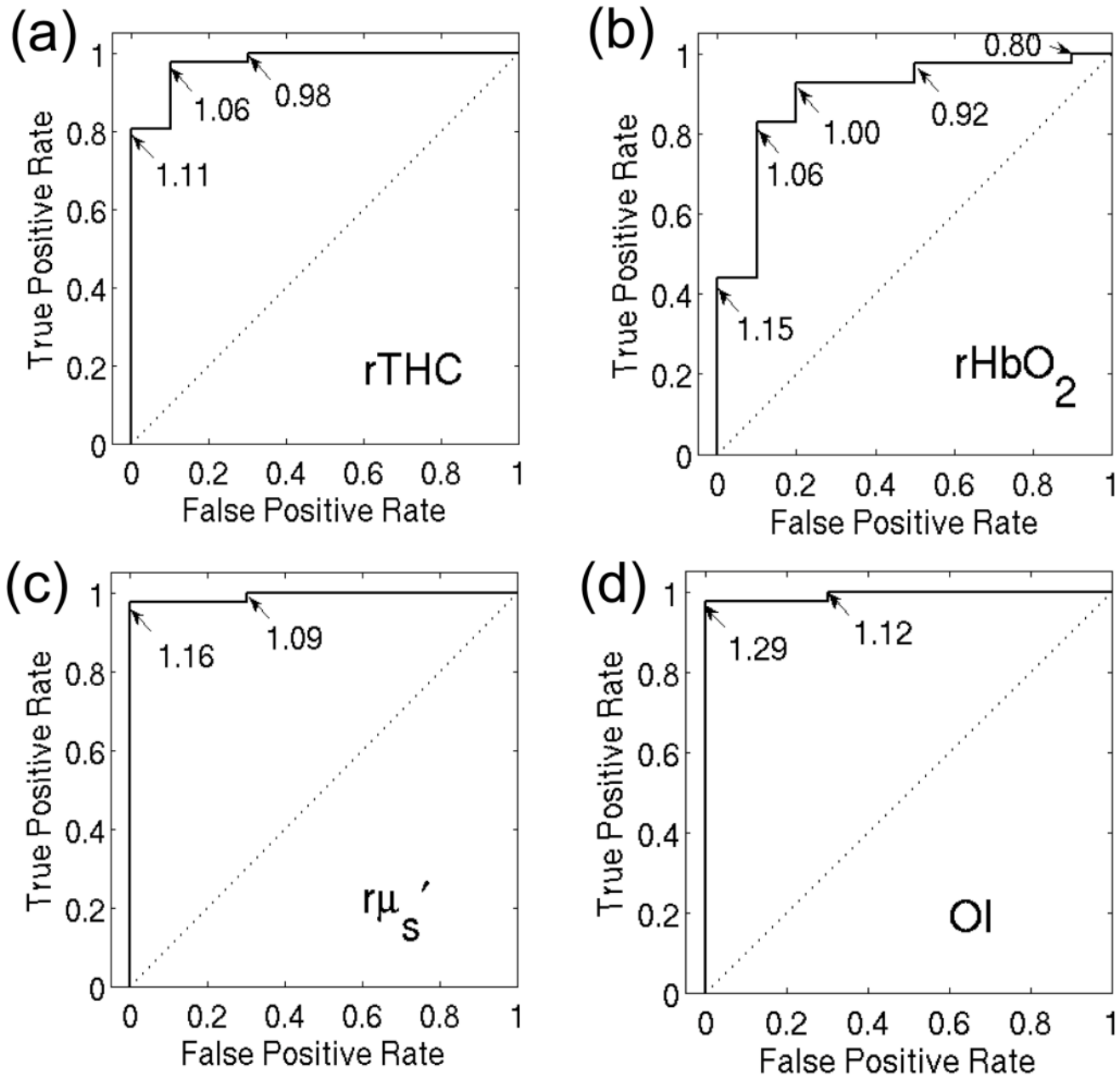

FIG. 6.

Receiver operating characteristic curves for *rTHC*, $rHbO_2$, $r\mu_s'$ and *OI* showing true positive rate for malignant lesions versus false positive rate for benign lesions. These rates are calculated by imposing a cutoff value (i.e. numerical values on each curve). For example, if *rTHC* > 1.06 designates positive result, then true positive rate is 98% and false positive rate is 10%.

NIH-PA Author Manuscript

NIH-PA Author Manuscript

NIH-PA Author Manuscript

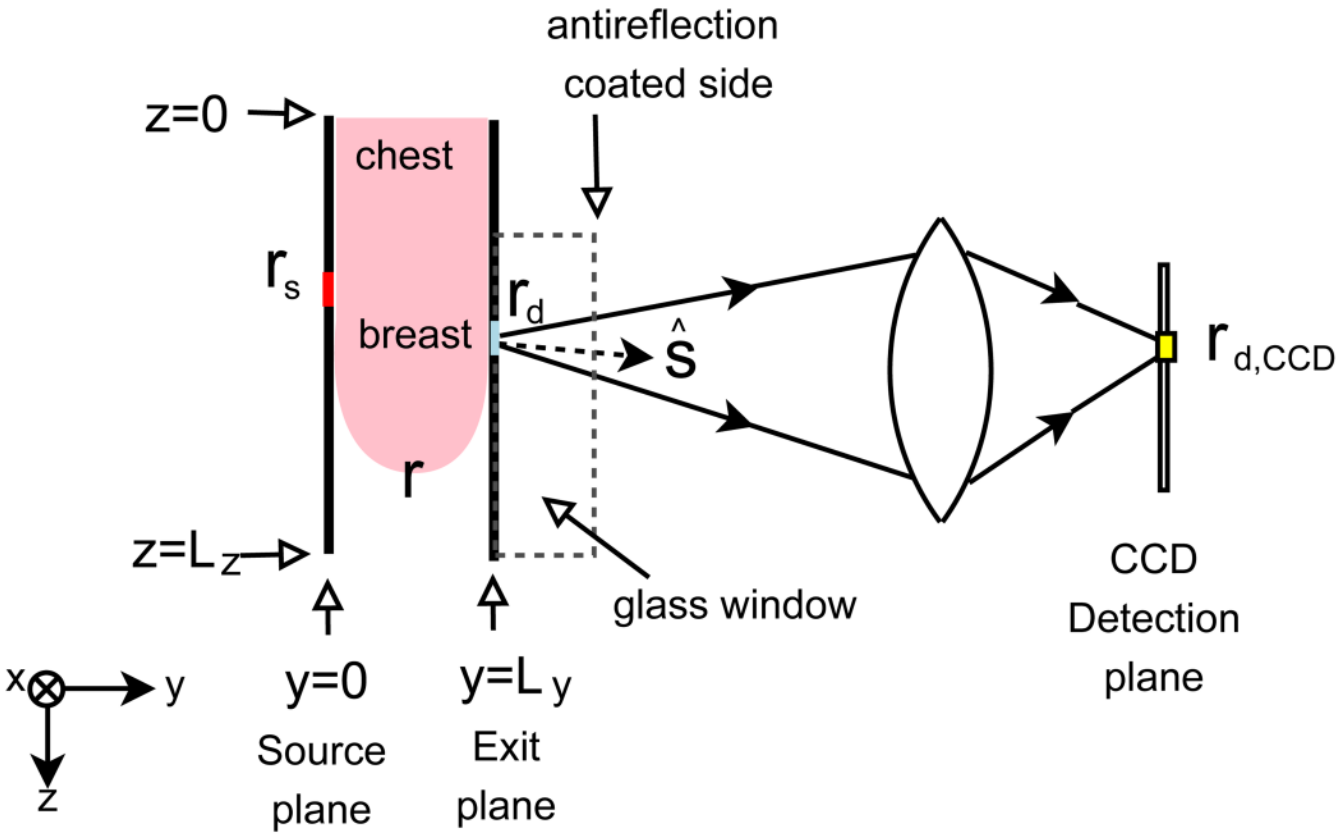

FIG. 7.
Schematic of breast DOT instrument.

NIH-PA Author Manuscript

NIH-PA Author Manuscript

NIH-PA Author Manuscript

TABLE I

Definition of extracted optical parameters from diffuse optical tomographic images. $\bar{X}_{(T)}$ and $\bar{X}_{(N)}$ are the mean values of variable X within tumor region and within normal region respectively. Optical Index is constructed based on these tumor-to-normal ratios of optical parameters.

Parameters	Abbreviation	Definition
Relative Total Hemoglobin Concentration	$rTHC$	$\bar{THC}_{(T)} / \bar{THC}_{(N)}$
Relative Blood Oxygen Saturation	$rStO_2$	$\bar{StO}_{2(T)} / \bar{StO}_{2(N)}$
Relative Deoxy-hemoglobin Concentration	rHb	$\bar{Hb}_{(T)} / \bar{Hb}_{(N)}$
Relative Oxy-hemoglobin Concentration	$rHbO_2$	$\bar{HbO}_{2(T)} / \bar{HbO}_{2(N)}$
Relative Scattering Coefficient (786nm)	$r\mu_s'$	$\bar{\mu}_{s'(T)} / \bar{\mu}_{s'(N)}$
Optical Index	OI	$rTHC \times r\mu_s' / rStO_2$

(T): tumor, (N): normal

NIH-PA Author Manuscript

NIH-PA Author Manuscript

NIH-PA Author Manuscript

TABLE II

Clinical characteristics of subjects, categorized by benign or malignant lesions. For continuous data such as age, mean ± standard deviation are shown. For each categorical variable, the number of women is shown. The percent of the total number of women in the group appears in parentheses.

Parameters	Subjects with benign lesions (n = 10)	Subjects with malignant lesions (n = 37)
Age (yr)	43 ± 10	48 ± 10
BMI (kg/m^2)	26 ± 5	27 ± 6
Menopausal status		
Pre-menopausal	6 (60%)	19 (51%)
Post-menopausal	4 (40%)	18 (49%)
Race		
Caucacian	7 (70%)	29 (78%)
African American	1 (10%)	6 (16%)
Asian	1 (10%)	1 (3%)
Hispanic	1 (10%)	1 (3%)
Mammographic density		
almost entirely fat	1 (10%)	2 (5%)
scattered fibroglandular densities	3 (30%)	9 (24%)
heterogeneously dense	3 (30%)	20 (54%)
extremely dense	1 (10%)	1 (3%)
unknown	2 (20%)	5 (14%)
Lesion size(cm)	1.7 ± 1.7	2.1 ± 1.2

NIH-PA Author Manuscript

NIH-PA Author Manuscript

NIH-PA Author Manuscript

TABLE III

Pathologic characteristics of 51 lesions measured with diffuse optical tomography (DOT) before or after core-biopsy.

Histopathologic Diagnosis	No. of lesions measured by DOT before core-biopsy (n = 30)	No. of lesions measured by DOT after core-biopsy (n = 21)
Malignant (n = 41)		
Invasive ductal carcinoma	16	20
Invasive lobular carcinoma	2	0
Ductal carcinoma *in situ*	2	1
Benign (n = 10)		
Fibroadenoma	4	0
Cyst	3	0
Fibrocystic	1	0
Lobular carcinoma *in situ*	2	0

NIH-PA Author Manuscript NIH-PA Author Manuscript NIH-PA Author Manuscript

TABLE IV

Mean (95% Confidence Interval) of extracted relative DOT parameters for three different lesion groups, and *P*-values testing three different types of hypotheses. P_a is the measure for difference between tumor and normal tissue. P_b is the measure for difference between malignant groups measured before (MalBcb) and after core-biopsy (MalAcb). P_c is the measure for difference between benign and malignant groups. An asterisk indicates that the difference is statistical significant ($P_x < 0.05$).

	Benign		Malignant before core-biopsy		Malignant after core-biopsy		Biopsy Effect	Benign vs Malignant
Parameter	**mean (95% CI)**	P_a	**mean (95% CI)**	P_a	**mean (95% CI)**	P_a	P_b	P_c
rTHC	0.98 (0.89–1.09)	0.56	1.16 (1.08–1.25)	0.01*	1.19 (1.10–1.28)	0.01*	0.45	0.01*
$rStO_2$	0.96 (0.86–1.08)	0.27	0.98 (0.90–1.06)	0.38	0.97 (0.90–1.05)	0.22	0.71	0.13
$rHbO_2$	0.94 (0.80–1.11)	0.25	1.14 (1.01–1.28)	0.04*	1.15 (1.03–1.29)	0.03*	0.79	0.02*
rHb	1.11 (0.85–1.45)	0.23	1.18 (0.98–1.43)	0.06	1.24 (1.03–1.49)	0.04*	0.54	0.32
$r\mu_s'$	0.98 (0.77–1.25)	0.79	1.53 (1.28–1.83)	0.01*	1.53 (1.28–1.84)	0.01*	1.00	0.005*
OI	1.04 (0.76–1.41)	0.67	1.83 (1.43–2.35)	0.01*	1.84 (1.43–2.37)	0.01*	0.96	0.004*

NIH-PA Author Manuscript

NIH-PA Author Manuscript

NIH-PA Author Manuscript

TABLE V

Area under curve (AUC), Odds ratios (OR) of lesion being malignant versus benign for a 0.10 (10%) increase in the value of the optical parameter. Asterisks are associated with $P < 0.05$ to indicate statistical significance.

Parameter	AUC	OR (95% CI)	*P*
rTHC	0.98	176 (3.3–9432)	0.01*
$rStO_2$	0.57	1.3 (0.5–3.0)	0.61
$rHbO_2$	0.90	4.3 (1.7–10.7)	0.001*
rHb	0.66	1.2 (0.9–1.7)	0.27
$r\mu_s'$	0.99	21.4 (1.4–333)	0.03*
OI	0.99	6.5 (1.3–33.3)	0.03*